Cell Stem Cell

Article

An *in vitro* menstrual cycle using organoids captures epithelial cell transitions during menstruation and regeneration of the human endometrium

Graphical abstract

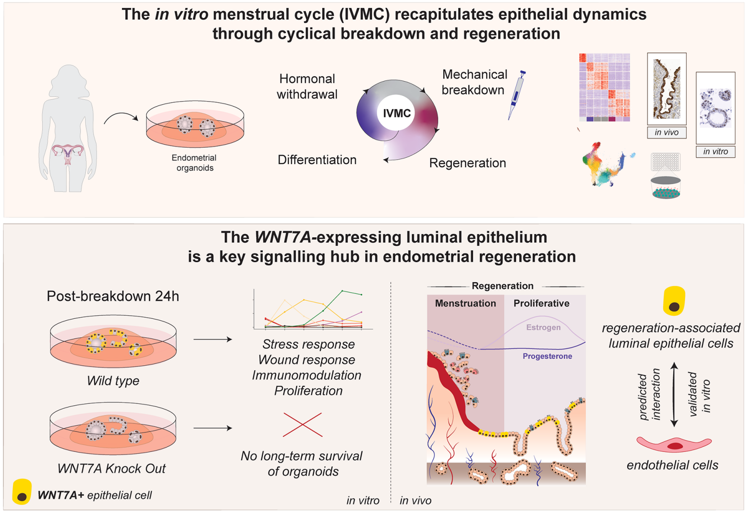

Highlights

- An organoid-based *in vitro* menstrual cycle captures breakdown and regeneration
- Breakdown induces a regeneration-associated luminal identity, marked by *WNT7A*
- Loss of WNT7A impairs long-term maintenance of endometrial organoids
- Regenerating epithelium signals to endothelial cells to promote wound healing

Authors

Konstantina Nikolakopoulou,
Weand Ybañez, Lhéanna Klaeylé, ...,
Hans-Rudolf Hotz, Charlotte Soneson,
Margherita Yayoi Turco

Correspondence

margherita.turco@fmi.ch

In brief

Turco and colleagues model the menstrual cycle *in vitro* using human endometrial organoids that undergo cycles of hormone-driven differentiation, including breakdown and regeneration occurring during menstruation, a process otherwise inaccessible in humans. They identify the *WNT7A*-expressing luminal epithelium as a key regenerative population in the endometrium.

Nikolakopoulou et al., 2026, Cell Stem Cell *33*, 1–16
May 7, 2026
https://doi.org/10.1016/j.stem.2026.04.005

Please cite this article in press as: Nikolakopoulou et al., An *in vitro* menstrual cycle using organoids captures epithelial cell transitions during menstruation and regeneration of the human endometrium, Cell Stem Cell (2026), https://doi.org/10.1016/j.stem.2026.04.005

Cell Stem Cell

CellPress
OPEN ACCESS

Article

An *in vitro* menstrual cycle using organoids captures epithelial cell transitions during menstruation and regeneration of the human endometrium

Konstantina Nikolakopoulou,[1,2] Weand Ybañez,[1,2] Lhéanna Klaeylé,[1] Lisa Frugoli,[1,2] Tereza Cindrova-Davies,[3] Hans-Rudolf Hotz,[1,4] Charlotte Soneson,[1,4] and Margherita Yayoi Turco[1,5,*]
[1]Friedrich Miescher Institute for Biomedical Research, Basel, Switzerland
[2]University of Basel, Basel, Switzerland
[3]Loke Centre for Trophoblast Research, University of Cambridge, Cambridge, UK
[4]SIB Swiss Institute of Bioinformatics, Basel, Switzerland
[5]Lead contact
*Correspondence: margherita.turco@fmi.ch

https://doi.org/10.1016/j.stem.2026.04.005

SUMMARY

Menstruation is an unusual process in which the human endometrium undergoes cyclical shedding with scarless regeneration. Despite its pivotal role in reproductive health, the cellular states and interactions orchestrating this process remain poorly defined, largely due to the lack of *in vitro* systems that capture the inaccessible perimenstrual window. We use human endometrial organoids to establish an *in vitro* menstrual cycle (IVMC) protocol that recapitulates cyclical epithelial dynamics. We validate the IVMC by benchmarking against *in vivo* samples spanning the menstrual window through histology, transcriptomic, and multiplex secreted-protein analysis. During menstruation, the *in vivo* luminal epithelium acquires a distinct transcriptomic signature, characterized by *WNT7A* expression. Loss of WNT7A compromises long-term organoid survival, highlighting its functional importance. The regeneration-associated luminal epithelium acts as a signaling hub during regeneration through interactions with the vasculature. This work opens new avenues to dissect the unique regenerative program of the endometrium in health and disease.

INTRODUCTION

Menstruation is a remarkable physiological process in which the uterine mucosa, the endometrium, repeatedly sheds and regenerates with no scarring. This cyclical process is tightly regulated by the ovarian hormones, estrogen, and progesterone (Figure 1A).[1] During each menstrual cycle, the endometrium faces a binary fate. If implantation occurs, the upper functional layer is maintained and differentiates into the decidua, which is essential to support pregnancy. In contrast, in the absence of implantation, regression of the corpus luteum causes a sharp decline in progesterone, which initiates menstruation, followed by regeneration of the entire mucosa.[1] This process is limited to a few species (mainly higher primates) and correlates with the extent of intrusion of the blastocyst into the uterine mucosa, which is most extreme in humans.[2]

Current knowledge regarding events surrounding the perimenstrual window comes primarily from tissue-level observations, showing that menstruation involves local hypoxia, cytokine release (IL-8 and COX2), infiltration of neutrophils and macrophages, and production of matrix metalloproteases by both immune and stromal cells, which promote degradation of the extracellular matrix and tissue sloughing.[1] Rapid re-epithelialization of the denuded surface is followed by restoration of the stroma and vasculature to fully regenerate the functional layer.[3] Studying menstruation has been challenging due to the difficulties in accessing the endometrium during the menstrual window (∼5 days) and modeling the process *in vitro*.

In this study, we focus on the epithelial compartment because it is the principal responder to breakdown, and re-epithelialization is the critical first step to restore the mucosal barrier.[3] The basal portion of the glands, which are not shed during menstruation, has been considered the main source of cells for epithelial regeneration.[3,4] However, other evidence suggests luminal cells could also contribute to re-epithelialization, as well as potentially serving as another reservoir of stem/progenitor cells.[5–7] How distinct epithelial states emerge, and transition during regeneration, and how the epithelium coordinates with other cell types to achieve this process remain unresolved.

We have deliberately taken a reductionist approach using tissue-derived endometrial organoids (EOs), which are a reproducible, hormone-responsive model of the epithelium, allowing investigation of autonomous mechanisms and their dynamics without confounding factors present in co-culture systems.[8–10] Here, we establish a straightforward, robust *in vitro* menstrual cycle (IVMC) protocol that captures all phases of the cycle

Please cite this article in press as: Nikolakopoulou et al., An *in vitro* menstrual cycle using organoids captures epithelial cell transitions during menstruation and regeneration of the human endometrium, Cell Stem Cell (2026), https://doi.org/10.1016/j.stem.2026.04.005

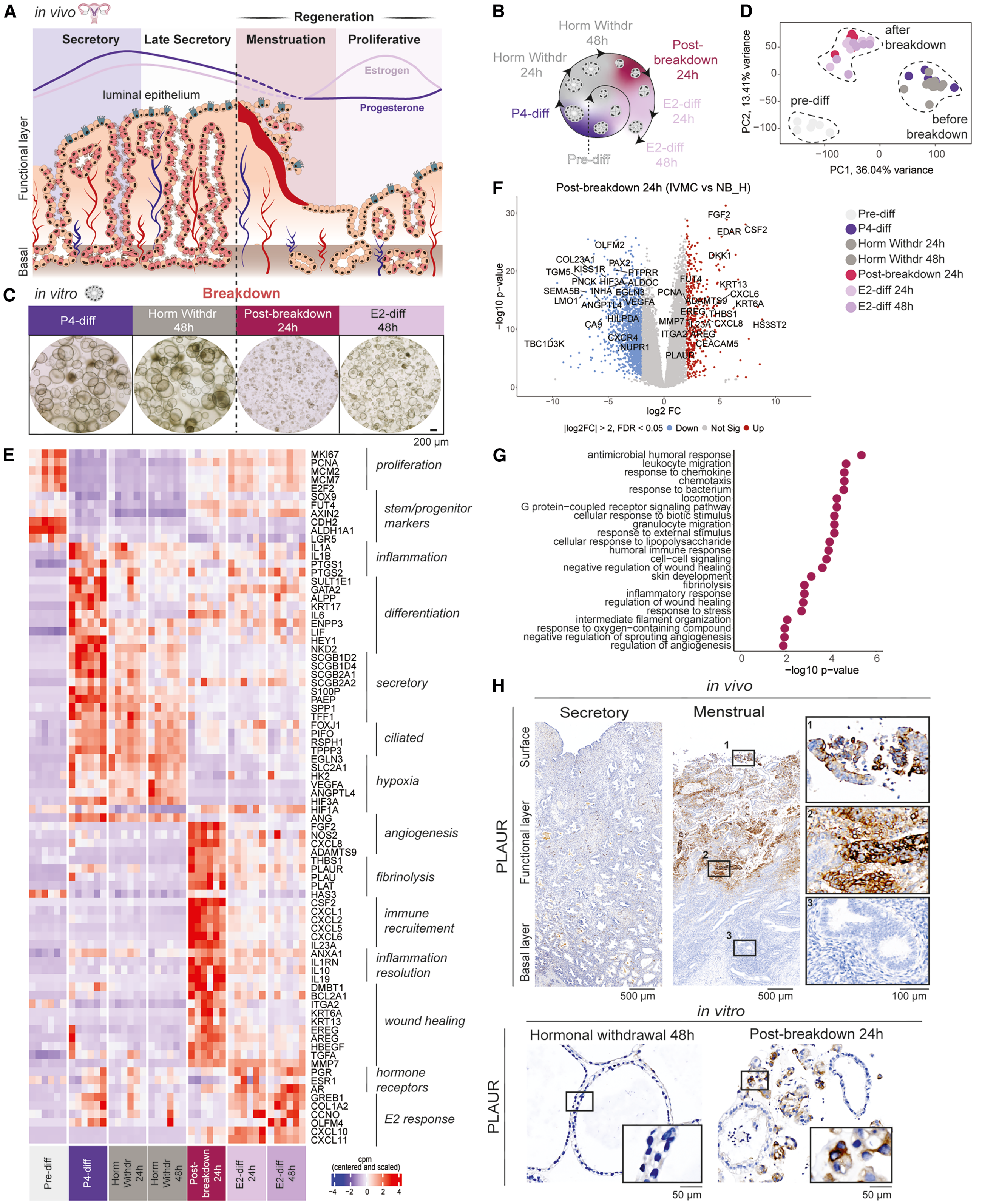

Figure 1. An IVMC recapitulates the dynamics of the endometrial epithelium through cyclical breakdown and regeneration

(A) Schematic of the morphological changes of the human endometrium and fluctuation of ovarian hormones across the menstrual cycle.

(B) Schematic of the different phases of the IVMC protocol.

(legend continued on next page)

Please cite this article in press as: Nikolakopoulou et al., An *in vitro* menstrual cycle using organoids captures epithelial cell transitions during menstruation and regeneration of the human endometrium, Cell Stem Cell (2026), https://doi.org/10.1016/j.stem.2026.04.005

compared with our previous single-round hormonal stimulation protocol.[8] This uniquely allows investigation of epithelial dynamics across repeated cycles, particularly during breakdown and regeneration occurring in the otherwise inaccessible perimenstrual window.

RESULTS

An IVMC protocol recapitulates the dynamics of the endometrial epithelium through cyclical breakdown and regeneration

To study epithelial dynamics during the perimenstrual window, we first developed an IVMC protocol that captures epithelial breakdown and regeneration across repeated cycles (Figure 1B). Building on our previous protocol for expansion and differentiation of EOs, we have now incorporated the critical phases of (1) hormonal withdrawal, (2) mechanical breakdown, and (3) regeneration, enabling analysis of key time points across this window (Figure 1B).[8] To this end, established cultures of EOs were first dissociated into single cells and cultured under standard expansion conditions in the absence of hormones until organoids formed. This time point marks the beginning of the first cycle of the IVMC protocol (Pre-differentiation, Pre-diff). EOs were then differentiated with estrogen (E2) and progesterone (P4) as we have previously described, to simulate the transition from proliferative to secretory phase (P4-diff).[8] The following steps then span the perimenstrual window: (1) hormones were withdrawn for 24 and 48 h (Horm Withdr 24 h and Horm Withdr 48 h) to mimic the demise of the corpus luteum, (2) hormone-withdrawn EOs were mechanically disrupted directly in their Matrigel droplets through pipetting to mimic the breakdown of the extracellular matrix by stromal and immune cells *in vivo*,[11,12] and (3) the fragmented EOs were replated in the absence of hormones for 24 h (Post-breakdown 24 h) to simulate the regenerative phase, followed by (4) exposure to E2 for 24 and 48 h (E2-diff 24 h and E2-diff 48 h) to mimic the start of the proliferative phase (Figures 1B and 1C). Morphological changes are obvious throughout this process, with small, cystic EOs being seen at Post-breakdown 24 h and increasing in size by E2-diff 48 h (Figure 1C). Consistent with these morphological changes, qRT-PCR across three consecutive cycles showed periodic expression patterns of markers of differentiation (*SCGB2A2* and *FOXJ1*) and proliferation (*MKI67*) at the expected time points (Figure S1A).

To validate that our IVMC protocol recapitulates epithelial changes throughout the menstrual cycle *in vivo*, we performed bulk RNA sequencing using EO lines from six healthy donors to account for human variability (Table S1). Control conditions included: (1) EOs not broken down but treated with hormones (NB_H), (2) EOs broken down but not treated with hormones (B_NH), and (3) EOs neither broken down nor treated with hormones (NB_NH) (Figure S1B). Clear morphological differences are observed between hormone-treated and untreated conditions, with secretions present only in hormone-treated EOs (Figure S1B). The major transcriptomic differences are due to mechanical disruption seen in all conditions and time points, as shown by principal component analysis (PCA) (Figure S1C). Hormonal treatment contributes to secondary segregation (Figure S1D). There is a distinct clustering corresponding to the differentiation status and response to breakdown (Figure 1D), with distinct gene expression patterns associated with each phase of the IVMC protocol (Figure S1E).

Next, we profiled transcriptomic changes across the IVMC protocol and validated differentially expressed genes (DEGs) at specific time points by immunohistochemistry (IHC) using full-thickness human uterine samples from hysterectomies performed across the menstrual cycle. Pre-diff EOs have a proliferative signature (*MKI67* and *PCNA*) reflecting their state in WNT-active expansion conditions. They also express high levels of certain putative stem/progenitor markers (*CDH2* and *ALDH1A1*), whereas others (*AXIN2*, *SOX9*, and *FUT4*) are lower (Figures 1E and S2A–S2E).[13–16] Upon differentiation, there is an upregulation of receptivity-specific genes (*ENPP3*, *IL6*, and *LIF*), and those confirming the differentiation to the secretory (*PAEP*, *SPP1*, *S100P*, *SCGB2A1*, and *SCGB1D4*) and ciliated (*FOXJ1*, *PIFO*, and *TPPP3*) lineages (Figures 1E, S3A, and S3B).[17–20]

We next assessed the phases of the protocol corresponding to the perimenstrual window. Whilst the stromal compartment is the primary sensor of progesterone decline, it is unclear whether epithelial cells respond to hormonal withdrawal.[12] Comparison of the expression profiles from EOs between P4-diff and Horm Withdr 48 h time points revealed 41 upregulated and 63 downregulated genes, indicating that the epithelial response to hormonal withdrawal is relatively modest (Figure S3C). However, key patterns were evident with secretory genes being downregulated while expression of ciliated genes persists (Figure 1E).

Hypoxia is a feature of the perimenstrual window.[21] While *HIF1A* is maximally induced at Post-breakdown 24 h, several hypoxia-associated genes (downstream targets of HIF1A) are upregulated at Horm Withdr 48 h (Figures 1E and S1F). For example, *VEGFA* expression increases after differentiation (P4-diff) and remains high during Horm Withdr 24 h and 48 h (Figure S1F), a pattern that was also confirmed at the protein level (Figure S1G). In contrast, genes involved in angiogenesis (*CXCL8*, *FGF2*, and *PDGFB*), vascular modulation (*EDN1*, *NOS1*, *NOS2*, and *NOS3*), and iron metabolism (*HMOX1* and

(C) Representative brightfield images of EOs across different phases of the IVMC protocol. Scale bar, 200 μm.

(D) PCA of batch corrected samples in the IVMC protocol analyzed by bulk RNA sequencing, colored by time point (n = 6 independent EO lines).

(E) Heatmap depicting centered and scaled counts per million (cpm) of selected genes across batch-corrected samples in the IVMC protocol.

(F) Volcano plot highlighting selected DEGs of EOs in the Post-breakdown 24 h time point of the IVMC protocol compared with control EOs (NB_H).

(G) Biological processes enriched in the Post-breakdown 24 h time point of the IVMC protocol, using genes upregulated in F.

(H) Representative IHC images for PLAUR in sections from endometrial tissue of the secretory and menstrual phases (n = 3 donors for each phase) and EOs at Horm Withdr 48 h and Post-breakdown 24 h (n = 4 independent EO lines). Scale bars of tissue sections, 500 μm and magnification, 100 μm. Scale bars of EO sections, 50 μm. Boxed areas of the EO sections are three times magnified.

Abbreviations are as follows: IVMC, *in vitro* menstrual cycle; Pre-diff, Pre-differentiation; P4-diff, progesterone differentiation; Horm Withdr, Hormonal Withdrawal; E2-diff, estrogen differentiation; NB_H, No Breakdown_Hormones.

TFRC) are upregulated at Post-breakdown 24 h (Figure S1F). This demonstrates the strength of the IVMC protocol in allowing the dissection of dynamic processes that can occur concurrently *in vivo* into discrete and experimentally accessible stages.

At Post-breakdown 24 h, gene expression shifts toward a wound-healing response, distinct from the proliferative Pre-diff state. In terms of putative stem/progenitor markers, EOs express high levels of *SOX9* and *FUT4* and downregulate *ALDH1A1*, *CDH2*, and *AXIN2*, indicating that these are distinct cell states (Figures 1E and S2A–S2E). The wound-healing signature includes genes encoding for cytokines that recruit immune cells (*CXCL1*, *CXCL6*, *CXCL8*, and *IL23*), growth factors (*EREG*, *AREG*, and *HBEGF*), fibrinolytic enzymes of the plasminogen system (*PLAU*, *PLAT*, and *PLAUR*), tissue remodeling factors (*MMP7*, *ADAMTS9*, and *ITGA2*), and anti-inflammatory mediators (*IL1RN* and *IL19*) (Figures 1E–1G). Many of these are characteristic of the menstrual window.[22] PLAUR, the plasminogen activator receptor that plays a key role in fibrinolysis, is a hallmark of scarless endometrial regeneration.[23] PLAUR is localized to the shedding functional endometrial layer *in vivo*, and EOs express it specifically at Post-breakdown 24 h (Figure 1H). Among the genes induced at this crucial time point are *THBS1* and *KRT13*, mediators of wound healing in the intestine and the lung, although not previously described in the endometrium.[24,25] Here, we confirm their expression *in vitro* and *in vivo*, demonstrating the utility of this protocol as a discovery tool to uncover molecular mediators of endometrial regeneration (Figures 1F, S3D, and S3E).

To assess the role of hormonal treatment prior to breakdown in endometrial regeneration, we compared EOs at Post-breakdown 24 h with control EOs of the same time point that had not been hormone-exposed (B_NH) (Figure S3F). Hormone-primed EOs upregulated genes involved in acute phase inflammation (*SAA1*, *SAA2*, *SAA4*, and *TREM1*), regulators of inflammation (*IRAK3*, *IL10*, and *CCL20*) and mucosal homeostasis (*DUOX2* and *DUOXA2*) (Figures S3F and S3G). EOs subjected to the full IVMC protocol, combining hormonal treatment with mechanical breakdown, showed better recovery (Figure S3H), further underscoring the physiological relevance of our model.

Introducing estrogen is a crucial step to mimic the transition into the proliferative phase of the menstrual cycle. Re-exposure of EOs to estrogen for 48 h (E2-diff 48 h) indeed attenuates the gene signature associated with response to breakdown and reactivates the expression of proliferative markers and estrogen-responsive genes (*PGR*, *GREB1*, *COL1A2*, and *OLFM4*) (Figures 1E, S3I, and S3J). This confirms the shift into the proliferative phase and onset of the following cycle. Overall, the IVMC protocol faithfully recapitulates epithelial dynamics across repeated menstrual cycles, replicating key gene signatures observed *in vivo*.

Regenerating EOs after breakdown resemble the *in vivo* luminal epithelium of the menstrual and proliferative phases

To identify key drivers of epithelial regeneration, we mapped *in vivo* epithelial cell states to those represented in EOs in the IVMC protocol. We first integrated epithelial cells from our single-cell RNA sequencing (scRNAseq) dataset of endometrial biopsies and whole uteri with recently published datasets (Figure S4A).[9,26–29] These together span the entire menstrual cycle, including the menstrual phase (Figure S4B). We re-analyzed the integrated datasets and annotated the epithelial cells considering their: (1) temporal emergence across the menstrual cycle, (2) transcriptomic profiles and biological processes, and (3) expression of well-established marker genes, enabling us to identify distinct epithelial populations specific to each phase. We identify 14 epithelial clusters, 2 ciliated populations, and 12 non-ciliated (Figures 2A and 2B).

The ciliated populations align with previously annotated clusters and include a “pre-ciliated” population enriched during the proliferative phase (*FOXJ1*, *MCIDAS*, *CCNO*, *CDC20B*, *MAD2L1*, and *NEK2*) with cells in the G2M cell cycle phase (Figure S4C). There is also a mature “ciliated population” that expresses regulators of terminal differentiation of ciliated cells (*PIFO*, *RSPH1*, and *TPPP3*) (Figures 2B and 2C).[9,30]

Among the non-ciliated populations, we annotate two hormone-responsive clusters: “hormone-responsive PGR^{high},” abundant in the proliferative phase and aligning with high estrogen stimulation, and “hormone-responsive PGR^{low},” more abundant in the secretory phase and aligning with downregulation of the PGR receptor at this phase of the menstrual cycle.[31] We also identify secretory cell clusters, which we annotate as early, mid, or late, based on their temporal emergence. This classification corresponded to their abundance across secretory sub-phases and was reflected by increasing *PAEP* expression and decreasing expression of genes of the secretoglobin family (*SCGB2A1*, *SCGB2A2*, and *SCGB1D2*) from the “secretory early” to the “secretory late” population (Figures 2B and 2C).

We also annotate “cycling” cells based on their expression of markers of proliferation (*PCNA*, *MKI67*), and two clusters expressing “KRT5^{+}” and “MUC5B^{+},” which were annotated previously (Figure 2C).[9,30,32] We also identify a transcriptionally active cluster characterized by high intronic fraction and genes involved in RNA splicing (*PNN*, *CCNL1*, and *FUS*), and the Hippo signaling pathway (*TEAD1* and *WWC1*), which we annotate as "transcriptionally active" (Figures 2C and S4D). “VIM^{+}” is a cluster that emerges early in the cycle, which co-expresses the stromal marker vimentin (*VIM*) and epithelial marker *EPCAM* (Figures 2C, S4E, and S4F). VIM^{+} cells show phase-specific localization, appearing at the luminal surface in the secretory phase and within glands during menstruation (Figure S4G).

We also identify a cell state that has a gene signature of wound healing and regeneration (*PLAU*, *MMP7*, *CSF1*, *ITGA2*, *CD47*) (Figure 2C and 2D). This population dominates during the menstrual phase *in vivo* (~50% of cells), while its abundance drops drastically in the secretory phase (Figure 2B). *ITGA2*, which is involved in cell adhesion and migration and marks the luminal progenitor cells in the mammary gland, is highly expressed in this cluster.[33] ITGA2 is detected in both luminal and glandular cells during the menstrual phase, but it is not expressed in the luminal epithelium in the secretory phase (Figure S4H). *CD47*, another marker of this cluster, is implicated in murine intestinal wound healing and is more strongly detected in the luminal epithelium during the menstrual than in the secretory phase (Figure S4I).[34] We annotate this as “regeneration-associated luminal.” We define an additional cluster, which is abundant during the mid-secretory phase and expresses receptivity-associated genes (*IL6*, *ENPP3*, *PTGS*, and *SCGB1D2*) in keeping with

Please cite this article in press as: Nikolakopoulou et al., An *in vitro* menstrual cycle using organoids captures epithelial cell transitions during menstruation and regeneration of the human endometrium, Cell Stem Cell (2026), https://doi.org/10.1016/j.stem.2026.04.005

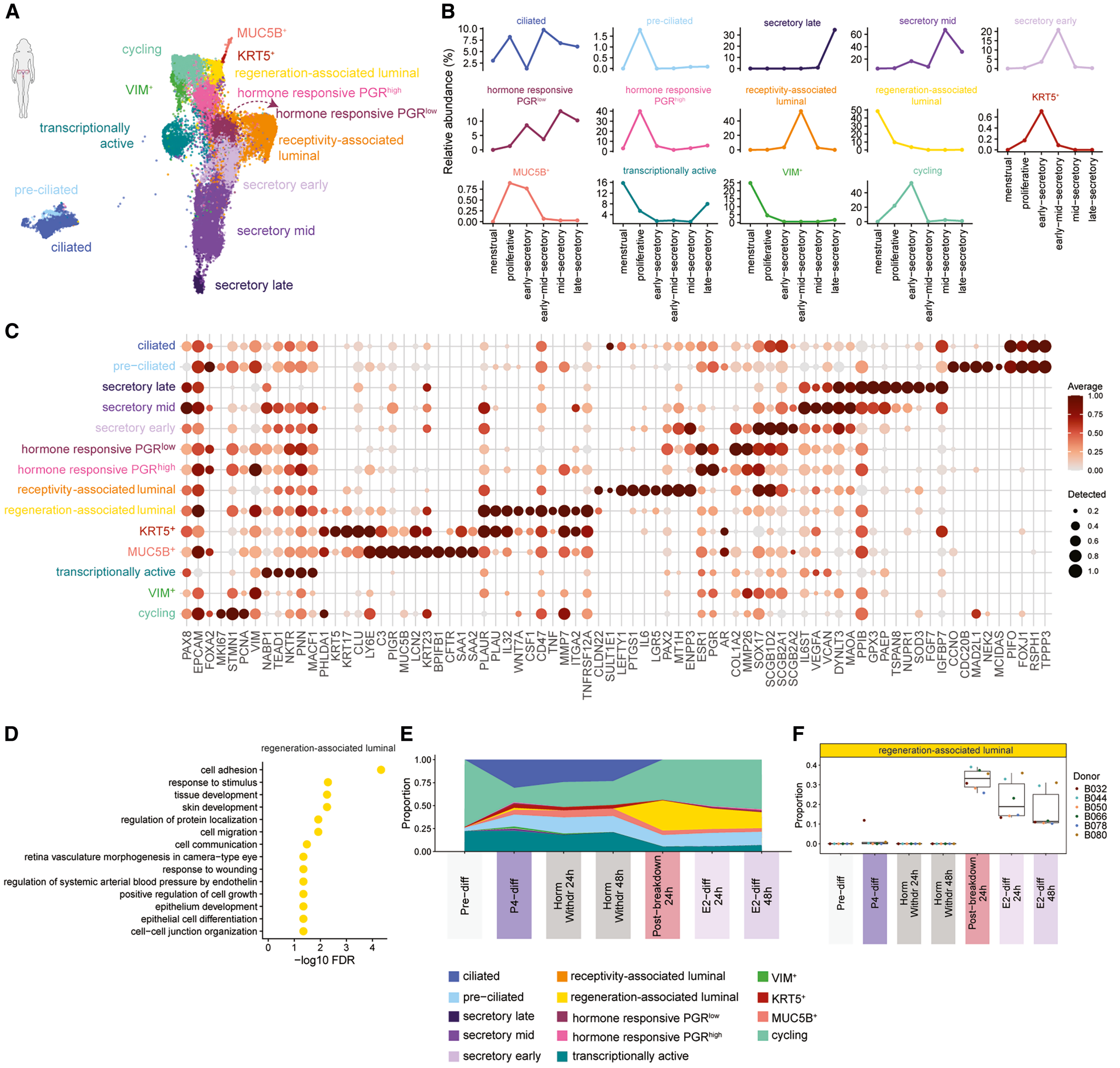

Figure 2. Regenerating EOs after breakdown resemble the *in vivo* luminal epithelium of the menstrual and proliferative phases

(A) Uniform manifold approximation and projection (UMAP) visualization of epithelial cell clusters from integrated scRNAseq data of endometrial tissue across the menstrual cycle ($n = 23$ donors).

(B) Relative abundance plots of *in vivo* epithelial cell clusters across phases of the menstrual cycle.

(C) Dot plot illustrating the expression of selected marker genes in each *in vivo* epithelial cell cluster. Dot size represents the proportion of expressing cells, while color denotes log2-transformed expression levels, normalized across all cell clusters.

(D) Biological processes enriched in the *in vivo* regeneration-associated luminal cluster using the top 100 marker genes.

(E) Area plot showing the relative abundance of the deconvolved *in vivo* epithelial cell clusters represented in EOs across the IVMC protocol, averaged across all donors.

(F) Box plot quantifying the estimated proportion of the *in vivo* regeneration-associated luminal cluster represented in EOs across the IVMC protocol. Individual dots represent individual donors ($n = 6$ independent EO lines).

roles in embryo implantation (Figures 2B and 2C).[17,18] We annotate this cluster as “receptivity-associated luminal.” We find that ENPP3 is present in the luminal epithelium in the secretory but less in the menstrual phase (Figure S4J). *LGR5*, previously described as a marker of the luminal epithelium, is also expressed in the receptivity-associated luminal cluster, with transcripts being detected in the secretory but not menstrual phase (Figures 2C and S4K).[7,9,30]

Please cite this article in press as: Nikolakopoulou et al., An *in vitro* menstrual cycle using organoids captures epithelial cell transitions during menstruation and regeneration of the human endometrium, Cell Stem Cell (2026), https://doi.org/10.1016/j.stem.2026.04.005

We next interrogated the cell states associated with epithelial regeneration, performing a deconvolution analysis of our bulk RNAseq dataset across the IVMC time points using the re-analyzed *in vivo* epithelial scRNAseq dataset as a reference (Figure 2E). Cycling and regeneration-associated luminal clusters are the most abundant at the Post-breakdown 24 h time point in all EO lines (Figure S4L). Whilst the proportion of cycling cells in EOs gradually increases in E2-diff 24 h and E2-diff 48 h phases (Figure 2E), the regeneration-associated luminal cluster is most abundant at Post-breakdown 24 h, representing ∼40% of the cells at this time point and then decreasing during E2-diff phases (Figures 2E and 2F). These findings provide transcriptional evidence of the dynamic nature of the luminal epithelium, shifting from a receptivity state in the secretory phase to a wound-healing program during menstruation.

WNT7A, a marker of the regeneration-associated luminal epithelium, is temporally associated with the response to breakdown *in vitro*

Our results uncover the temporary acquisition of a luminal-like transcriptional state during regeneration *in vitro*. We next sought to investigate what drives this response. Among the genes expressed in the regeneration-associated luminal cluster, *WNT7A*, a ligand of the WNT signaling pathway, is a potential candidate for its role in epithelial regeneration (Figure 3A).[35] Indeed, we detect *WNT7A* transcripts *in vivo* on the luminal epithelium undergoing menstruation, revealing that its expression precedes the proliferative phase (Figure 3B). Interrogation of *WNT7A* dynamics across the IVMC protocol reveals a transient peak in expression at Post-breakdown 24 h compared with low expression in EOs that did not undergo breakdown (NB_H) (Figure 3C). This pattern is consistently observed in EOs in continuous menstrual cycles (Figure 3D). Spatially, *WNT7A* transcripts are undetectable in EOs at Horm Withdr 48 h but are uniformly present at Post-breakdown 24 h (Figures 3E and 3F). *WNT7A* is also the dominant WNT ligand expressed in EOs at Post-breakdown 24 h (Figure 3G).

WNT7A is essential for glandular development in mice and has been implicated in endometrial regeneration in primates.[35,36] To investigate whether WNT7A has a direct effect on the human epithelium, we generated *WNT7A* knockout (KO) organoids using CRISPR gene editing and assessed the impact on epithelial regeneration. Long-term survival of *WNT7A* KO clones is severely compromised compared with wild-type (WT) clones (Figures 3H and 3I). Clonal cultures cannot be expanded beyond 5–7 passages after their establishment (Figure 3H). The overall growth potential, defined by the ability to expand and freeze down clones, is lower in *WNT7A* KO clones (Figure 3J). This highlights the critical role of WNT7A in epithelial renewal and provides functional evidence for its requirement for regeneration upon breakdown.

Transient ciliated and non-ciliated states emerge during regeneration, with *WNT7A* bridging breakdown to proliferation

Having pinpointed *WNT7A*-expressing cells as critical for long-term epithelial maintenance *in vitro*, we next investigated the emergence of distinct epithelial states during the transition from breakdown to regeneration and how these cell states relate to *WNT7A* expression. We performed scRNAseq of three independent EO lines (Table S1), and adjusted our *in vitro* protocol with finer time resolution to capture this crucial regenerative window: 48 h after hormonal withdrawal (Horm Withdr 48 h), 12, 24, 48 h after breakdown (Post-breakdown 12 h, Post-breakdown 24 h, Post-breakdown 48 h) and 24 and 48 h after treatment with estrogen (E2-diff 24 h and E2-diff 48 h) (Figures 4A and S5A). We identify 16 distinct clusters, comprising seven ciliated and nine non-ciliated sub-clusters (Figure 4B). Before breakdown (Horm Withdr 48 h), both "ciliated" and secretory cells ("secretory SCGB^{high}" and "secretory PAEP^{+}") are abundant, with ciliated cells dominating, consistent with our earlier observation that their markers persist after hormonal withdrawal, unlike secretory markers (Figures 1E and 4C).

In the immediate response to breakdown, non-ciliated "stress responsive" clusters appear at Post-breakdown 12 h, characterized by high expression of heat shock proteins (*HSPA1A* and *DNAJB1*) (Figures 4D and S5B). By 24 h, "ciliated stress responsive" cells also appear, expressing unfolded protein response genes (*CRELD2* and *DNAJB11*), indicative of a cellular adaptation to stress (Figures 4D and S5B). In parallel, we detect both ciliated and non-ciliated "wound responsive 12 h" clusters marked by expression of injury-responsive genes (*TNFRSF12A* and *SFN*), tissue remodeling factors (*F3* and *FGF2*), and ribosome biogenesis and rRNA processing genes (*LYAR* and *RRS1*) (Figures 4D and S5B). By Post-breakdown 24 h, both ciliated and non-ciliated cells adopt a distinct "wound responsive 24 h" signature enriched for genes involved in wound healing processes (*PLAUR*, *CXCL8*, *KRT17*, and *MMP7*) (Figures 4D and S5B), consistent with our bulk RNAseq analysis (Figure 1E). *WNT7A* expression is tightly coupled to the induction of the wound-response program in both ciliated and non-ciliated cells, as it is completely absent from the "stress responsive" clusters, expressed at low levels in the earlier "wound responsive 12 h" clusters, and strongly induced in the "wound responsive 24 h" cluster (Figure 4E).

At Post-breakdown 48 h, epithelial states diversify, indicating a shift from a common wound-response shared across cell types to more specialized states. Among the distinct clusters, we identify a distinct "OxPhos-high" cluster enriched in genes involved in oxidative phosphorylation and markers of the regeneration-associated luminal epithelium *in vivo* (*IL32*, *MMP7*, *CD47*, and *KRT17*), including *WNT7A* (Figures 4D and S5B). Clusters with immune-related function also emerge, characterized by genes of the TNF family (*TNF* and *TNFAIP2*), cytokines (*CXCL10* and *LIF*), cytokine receptors (*IL1R1*), and acute inflammatory response genes (*SAA1* and *SAA2*) (Figures 4D and S5B). We annotate those as "immunomodulatory." The first appearance of "cycling" cells (S/G2M phases), which continue to express *WNT7A*, at this time point marks a critical turning point from wound response to proliferative regeneration (Figures 4D, S5B, and S5C). Most proliferative cells arise in the non-ciliated population (20%) with fewer in the ciliated lineage (<2%) (Figure S5B).

Following re-exposure to E2, a "hormone-responsive" population appears, marked by the expression of *ESR1* and *PGR* (Figures 4D and S5B). Within the ciliated compartment, E2 treatment increases the abundance of the "pre-ciliated" cell cluster (*FOXJ1*, *CCNO*, *MCIDAS*, and *CDC20B*) shown previously (Figures 4D and S5B).[37] The "pre-ciliated" cell cluster also

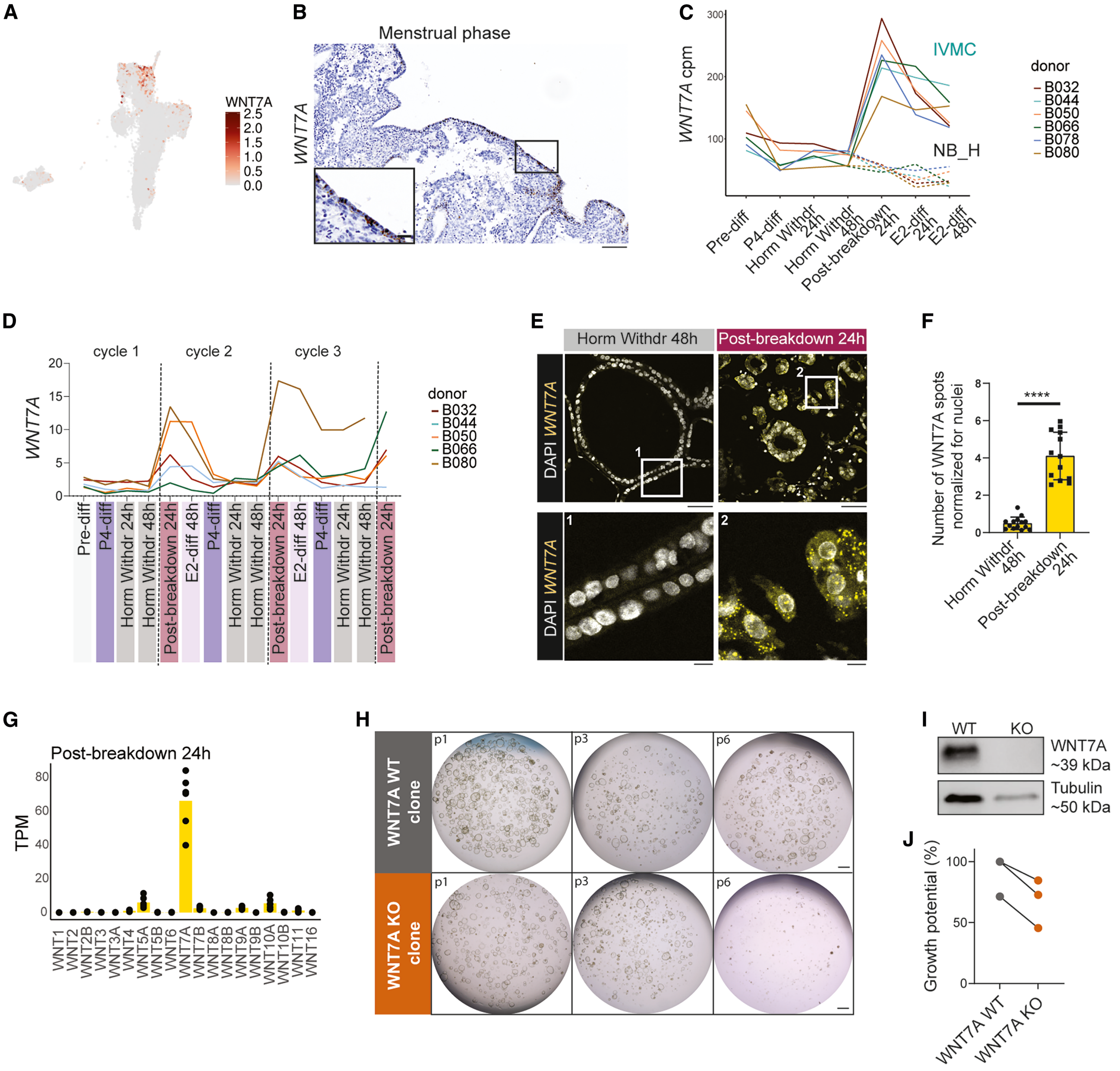

Figure 3. *WNT7A*, a marker of the regeneration-associated luminal epithelium, is temporally associated with the response to breakdown *in vitro*

(A) Uniform manifold approximation and projection (UMAP) visualization showing the $\log_2$-transformed expression of *WNT7A* across individual cells *in vivo*.

(B) *In situ* hybridization (ISH) showing localization of *WNT7A* transcripts in menstrual phase endometrium ($n = 1$ donor). Scale bars, 100 μm (main) and 50 μm (inset).

(C) Line plots depicting cpm of *WNT7A* in batch corrected samples from bulk RNAseq data. Solid lines represent expression in EOs undergoing the IVMC protocol. Dashed lines represent expression in control EOs NB_H, no breakdown hormones.

(D) qRT-PCR analysis of *WNT7A* expression of EOs undergoing continuous cycles of the IVMC protocol, normalized to housekeeping genes ($n = 5$ independent EO lines).

(E) ISH showing localization of *WNT7A* transcripts in EOs at Horm Withdr 48 h and Post-breakdown 24 h time points. Scale bars, 50 μm (main) and 10 μm (inset).

(F) Quantification of *WNT7A* ISH signal in E. Significance was assessed using unpaired *t* tests ($p \leq 0.0001$).

(G) Bar plot showing the average transcripts per million (TPM) of *WNT* ligands at Post-breakdown 24 h in EOs undergoing the IVMC protocol, analyzed with bulk RNAseq ($n = 6$ independent EO lines).

(H) Representative brightfield images of WNT7A WT and WNT7A KO clones over six passages. Scale bars, 500 μm.

(I) Western blot for WNT7A protein in WNT7A WT and WNT7A KO clones depicted in H.

(J) Percentage of WNT7A WT and WNT7A KO clones that could be frozen down as an estimate of growth potential ($n = 3$ independent EO lines).

Please cite this article in press as: Nikolakopoulou et al., An *in vitro* menstrual cycle using organoids captures epithelial cell transitions during menstruation and regeneration of the human endometrium, Cell Stem Cell (2026), https://doi.org/10.1016/j.stem.2026.04.005

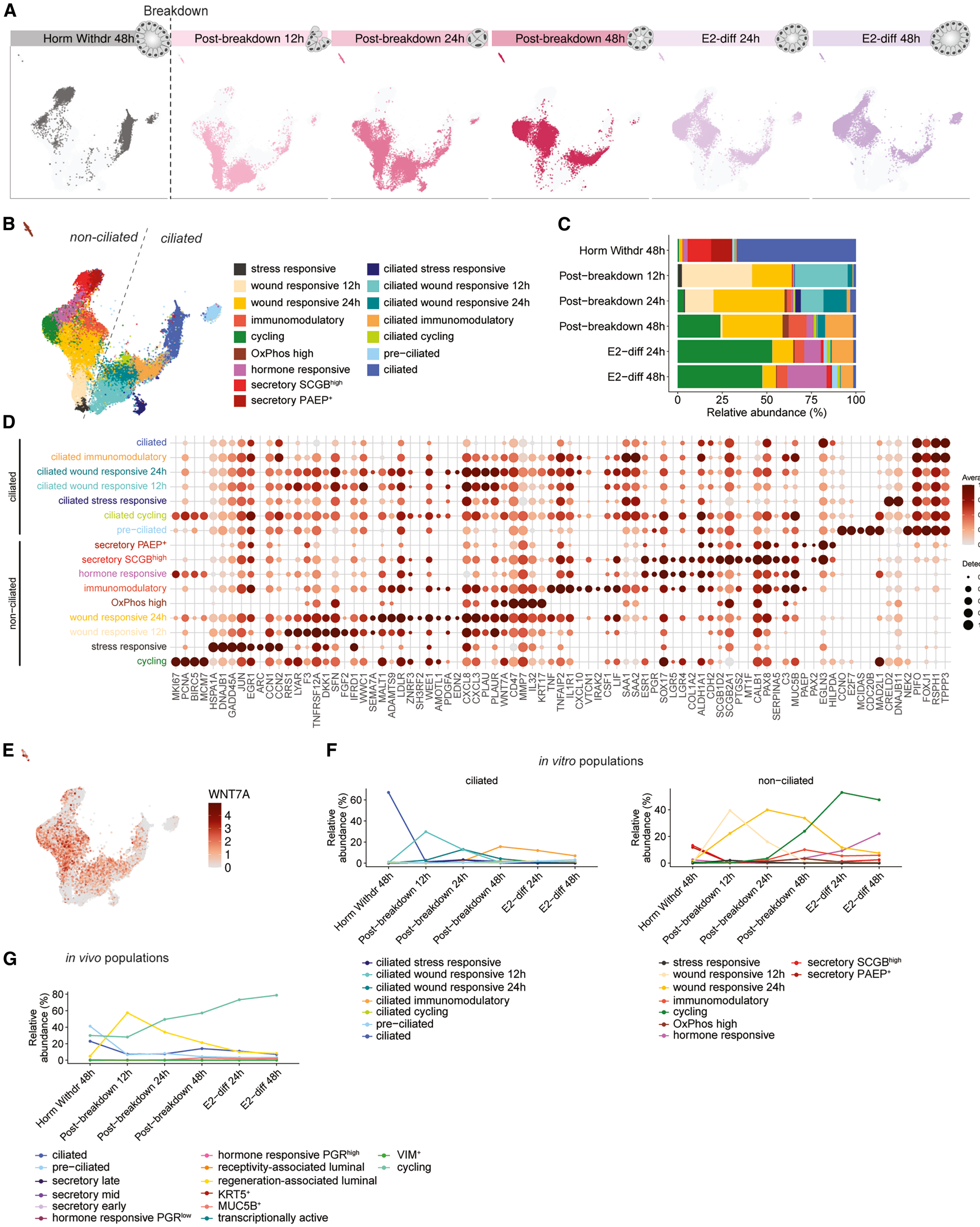

(legend on next page)

Please cite this article in press as: Nikolakopoulou et al., An *in vitro* menstrual cycle using organoids captures epithelial cell transitions during menstruation and regeneration of the human endometrium, Cell Stem Cell (2026), https://doi.org/10.1016/j.stem.2026.04.005

shows an enrichment for *E2F7*, a transcriptional regulator of canonical S-to-G2 progression that promotes multiciliated cell differentiation (Figure 4D).[38] These changes mirror the processes occurring during the proliferative phase *in vivo*. The global downregulation of *WNT7A* in these estrogen-responsive clusters suggests that its function is confined to the earlier hormone-independent regenerative stage (Figure 4D).

In response to breakdown, EOs gradually transition through states of an immediate stress response at 12 h followed by a wound-healing state, with *WNT7A* expression peaking at 24 h, and finally initiation of cell proliferation (Figures 4F and S5D). Interrogation of the *in vivo* epithelial identities in EOs undergoing the IVMC protocol further suggests that the *WNT7A*-expressing luminal identity is similarly enriched before the emergence of cycling cell states (Figure 4G). This highlights the temporal regulation of *WNT7A* in bridging the response of epithelial cells from breakdown to their proliferation, as also suggested by the inability of *WNT7A* KO organoids to survive long-term.

The regeneration-associated luminal epithelium acts as a signaling hub, particularly via interactions with endothelial cells

Our findings identify the transient *WNT7A*$^{+}$ *in vitro* population, resembling the *in vivo* regeneration-associated luminal epithelium, as a key mediator of the response to breakdown through signaling within the epithelial compartment. We next asked whether the regeneration-associated luminal epithelium communicates with other cell types during endometrial regeneration *in vivo*. To investigate this, we performed CellChat analysis on the "all-lineage" *in vivo* endometrial scRNAseq dataset, focusing on all cell states present in the menstrual and early proliferative phases of the cycle. Defining the regeneration-associated luminal as the sender population, the analysis predicts broad interactions not only with other epithelial populations but also with immune, stromal, and particularly endothelial cells via multiple signaling pathways (Figures 5A and 5B). Several of the identified ligands involved in pathways mediating these interactions were specifically upregulated in the EOs and detected in organoid-conditioned media at Post-breakdown 24 h (Figures 5C and 5D).

Within the epithelial compartment, WNT signaling emerges as a major pathway with *WNT7A* as the main ligand expressed by the regeneration-associated luminal epithelium (Figures 5B and S5E). *In vitro*, EOs upregulate both *FZD6* and *FZD10* at Post-breakdown 24 h (Figures S5F and S5G), with *FZD6* being broadly expressed and *FZD10* being limited to non-ciliated cell types and to only the cycling ciliated cells *in vitro* (Figure S5H). IL-6, a pleiotropic cytokine, is another mediator of intra-epithelial interactions *in vivo* (Figure 5B). Transcriptomic analysis of EOs and Luminex secretion analysis show upregulation of IL-6 at both P4-diff and Post-breakdown 24 h, suggesting a potential dual role in both endometrial receptivity and wound healing (Figures 5C and 5D).[18,39,40] Epithelial-stromal cell interactions in the perimenstrual window have not been widely explored. Our analysis predicts that midkine (MDK), epidermal growth factor (EGF), endothelin (EDN), and platelet-derived growth factors (PDGF) may act as mediators (Figures 5B–5D).

Interactions between epithelial cells and immune cells are likely to be critical, given the influx of neutrophils and macrophages during menstruation.[41] From our analysis, epithelial cells are predicted to interact extensively with myeloid populations via colony-stimulating factors (CSFs), complement 3 (C3), tumor necrosis factor (TNF), macrophage migration inhibitory factor (MIF), and annexin (ANXA1) (Figure 5B). Secretion of GM-CSF (encoded by *CSF2*) and TNFa by EOs at the Post-breakdown 24 h time point was confirmed by Luminex (Figure 5D). Furthermore, *ANXA1*, an established mediator of inflammation resolution essential for regeneration, is highly expressed in regeneration-associated luminal cells *in vivo* and upregulated at Post-breakdown 24 h *in vitro*, particularly in EOs subjected to the IVMC (Figures 5C, S5E, and S5I).[42]

The strongest interactions were identified between epithelial and venous cells, highlighting a prominent epithelial-endothelial axis during regeneration (Figure 5A). CXCL chemokines, GDF growth/differentiation factor 15 (*GDF15*), vascular endothelial growth factor A (*VEGFA*), adrenomodullin (*ADM*), leukemia inhibitory factor (*LIF*), nicotinamide phosphoribosyltransferase (*NAMPT*), semaphorins (*SEMA3A*, *SEMA3B*, and *SEMA3C*), *MDK*, and *TNF* are predicted to mediate these interactions (Figure 5B). *In vitro*, several CXCL family members are upregulated in EOs at the Post-breakdown 24 h time point, including *CXCL8*, previously reported for its role in angiogenesis during the perimenstrual window (Figure 5C).[43,44] EOs secrete high levels of IL-8 at Post-breakdown 24 h (Figure 5D). We validated the expression of atypical chemokine receptor 1 (ACKR1) on venous endothelial cells (Figure S5J) and CXCR1 on epithelial cells in menstrual tissue and *in vitro* (Figure S5K), suggesting potential autocrine and paracrine effects of IL-8.[43] EOs also secrete GROβ and FGFb at Post-breakdown 24 h, which may further reinforce epithelial-endothelial interactions during regeneration (Figure 5D).

To functionally validate the predicted epithelial-endothelial interactions, we performed wound healing assays using both an established human umbilical vein endothelial cell line (HUVECs) and primary human uterine microvascular endothelial cells (HUtMECs).

Figure 4. Transient ciliated and non-ciliated states emerge during regeneration, with *WNT7A* bridging breakdown to proliferation

(A) UMAP visualizations of cells colored for each time point in separate panels. EOs are subjected to the IVMC protocol and collected for scRNAseq before breakdown (Horm Withdr 48 h), after breakdown (Post-breakdown 12 h, 24 h, and 48 h), and after estrogen treatment (E2-diff 24 h and E2-diff 48 h) (*n* = 3 independent EO lines).

(B) UMAP visualization of cells colored by annotated clusters.

(C) Bar plot showing the relative abundance (in percentage) of each cell cluster in the different time points.

(D) Dot plot illustrating the expression of selected marker genes in each epithelial cell cluster. Dot size represents the proportion of expressing cells, while color denotes log2-transformed expression levels, normalized across all cell populations.

(E) UMAP visualization showing the $\log_2$-transformed expression of *WNT7A* across individual cells.

(F) Line plot showing the relative abundance (in percentage) of each *in vitro* cell cluster in the different time points.

(G) Line plot showing the relative abundance (in percentage) of each predicted *in vivo* cell cluster corresponding to cells across the different time points *in vitro*.

Please cite this article in press as: Nikolakopoulou et al., An *in vitro* menstrual cycle using organoids captures epithelial cell transitions during menstruation and regeneration of the human endometrium, Cell Stem Cell (2026), https://doi.org/10.1016/j.stem.2026.04.005

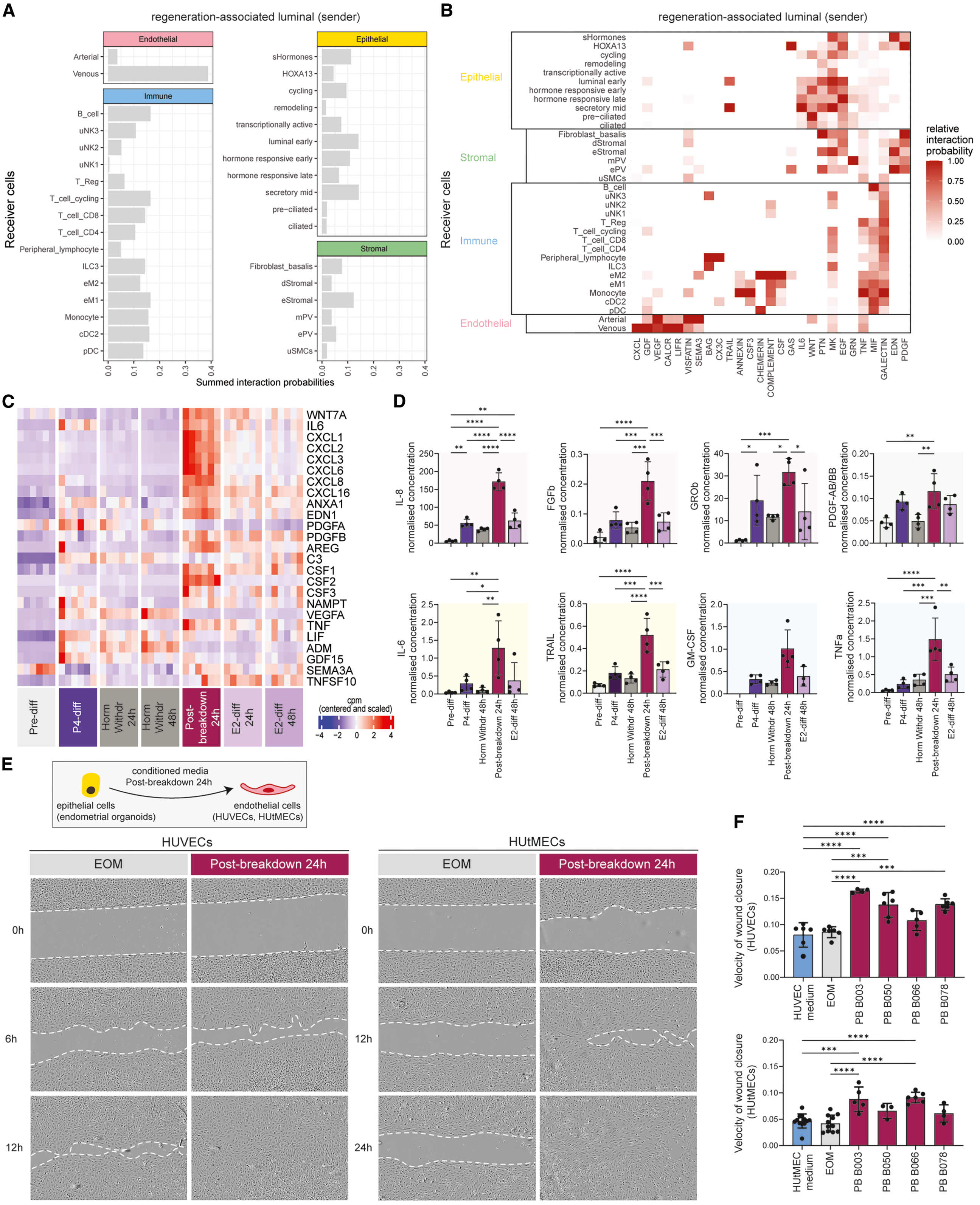

Figure 5. The regeneration-associated luminal epithelium acts as a signaling hub, particularly via interactions with endothelial cells

(A) Total estimated interaction probabilities between regeneration-associated luminal epithelial cells (sender) and all the other epithelial and non-epithelial cell clusters (receiver) *in vivo*.

(legend continued on next page)

Endothelial cells were treated with conditioned media from EOs at the Post-breakdown 24 h time point, which transcriptionally aligns with regeneration-associated luminal epithelial cells *in vivo*. We observed a significant increase in the velocity of endothelial wound closure in both cell types, after treatment with conditioned media from EOs from four independent donors (Figures 5E and 5F), highlighting the potential role of epithelial cells in mediating angiogenesis in response to breakdown *in vivo*.

DISCUSSION

Despite its central role in reproductive health, the process by which the endometrium regenerates after menstruation has remained a "black box," inaccessible to study *in vivo*. Here, we establish an IVMC protocol using EOs that recapitulates the sequential and cyclical changes of the endometrial epithelium during hormonal differentiation and withdrawal, breakdown, and regeneration. Our aim was to design a robust, reproducible protocol that (1) recapitulates the hallmarks of the menstrual window to physiologically connect one cycle to the next, (2) maintains epithelial dynamics of hormone responses across repeated cycles, and (3) can be readily implemented across laboratories.

To model the critical breakdown phase, we mechanically disrupted EOs, a simple and consistent approach that avoids the variability of enzyme-, conditioned media-, or co-culture-based methods, while still reflecting the piecemeal shedding of the superficial endometrium observed *in vivo*.[6] We uncover the transcriptional transitions in cell states that underpin epithelial regeneration *in vitro* and mapped these against *in vivo* reference to epithelial cell states across the cycle, with validation in full-thickness uterine tissue blocks that span the menstrual window. A major strength of this system is that it enables controlled, parallel analysis at high temporal resolution across multiple donors and experimental conditions, minimizing inter-individual variability that has confounded comparisons of biopsies or hysterectomy samples collected at different cycle stages.

The IVMC protocol establishes a comprehensive *in vitro* framework for studying menstruation and reveals key epithelial-intrinsic mechanisms underlying regeneration. Our data revealed an enrichment of the regeneration-associated luminal epithelial signature (*WNT7A*, *ITGA2*, and *CD47*) in EOs after breakdown. Although it remains to be experimentally confirmed whether this reflects an injury response or acquisition of a luminal cell state that directly contributes to regeneration into all the different lineages, previous studies support an active role of luminal epithelial cells in regeneration.[5–7] Scanning electron microscopy studies showed re-epithelialization from the unshed areas, and transcriptomic analyses of laser-captured shedding surface layers reveal expression of genes involved in tissue degradation and regeneration.[5,6] Because distinct cell states emerge during the IVMC protocol, including basal glandular markers (*CDH2* and *ALDH1A1*) that are highly expressed in pre-diff EOs and other putative progenitor markers (*FUT4* and *SOX9*) expressed after breakdown, it provides an opportunity to dissect the relative contributions of the different cell states in regeneration and their lineage relationships.[13–16]

WNT7A emerged as a defining marker of the regenerative window, as its expression is tightly linked to the luminal epithelium in the menstrual and proliferative phases. *WNT7A* is critical for uterine patterning,[45] postnatal gland formation[36] and anti-apoptotic function[46] in mice, whereas in primates WNT7A has been implicated in postmenstrual regeneration and secretory transformation.[35] In other adult tissues, WNT7A plays roles in epithelial integrity, maintenance of stem cells, wound healing, and inhibition of inflammatory stimuli through diverse mechanisms.[47–53] *In vitro*, genetic deletion of *WNT7A* in EOs impairs long-term survival, identifying *WNT7A* as an epithelial-derived factor that supports survival and regeneration following endometrial tissue breakdown. An outstanding question concerns the signaling through which WNT7A mediates these effects and in which cell types. WNT7A can activate both the canonical WNT signaling through FZD5 receptor and the non-canonical JNK-mediated pathway through FZD10 in the human endometrial adenocarcinoma Ishikawa cell line.[54] The inability of exogenous canonical WNT activators, present in our organoid growth medium, to rescue the WNT7A KO phenotype also suggests that WNT7A may act through β-catenin-independent mechanisms in the endometrium.[47,54]

Regeneration of the endometrium following menstrual breakdown requires coordinated renewal of different cell types. Our cell-cell communication analysis of all cells *in vivo* during the menstrual and proliferative phases predicted numerous interactions between regeneration-associated epithelial and non-epithelial populations, particularly with endothelial cells mediated by CXCL cytokines such as IL-8, a key regulator of angiogenesis.[43,44,55] We show that, consistent with these predictions, following breakdown, EOs secrete IL-8 together with other pro-angiogenic factors, including FGFb and GROβ, underscoring the physiological relevance of the IVMC protocol. We validated the predicted epithelial-endothelial crosstalk *in vivo* using an *in vitro* wound healing assay, demonstrating that primary endothelial cells (HUVECs and HUtMECs) close wounds more rapidly when exposed to EO-conditioned media. While our current system focuses on the epithelium, significant efforts in the field are directed at developing co-culture models of the endometrium to investigate cell-cell interactions and their impact on

---

(B) Heatmap showing the estimated relative interaction probabilities for different signaling networks between regeneration-associated luminal epithelial cells (sender) and all the other epithelial and non-epithelial cell clusters (receiver).

(C) Heatmap depicting centered and scaled cpm of ligands involved in pathways identified in B, across batch-corrected samples of EOs in the IVMC protocol.

(D) Bar plots showing the normalized concentration of IL-8 (*CXCL8*), FGFb (*FGF2*), GROb (*CXCL2*), PDGF-AB/BB (*PDGFB*), IL-6 (*IL6*), TRAIL (*TNFSF10*), GM-CSF (*CSF2*), and TNFa (*TNFA*) analyzed through a Luminex assay of supernatants of EOs subjected to the IVMC protocol (*n* = 4 independent EO lines). Statistical analysis was performed using ordinary one-way ANOVA. * $p \leq 0.05$, ** $p \leq 0.01$, *** $p \leq 0.001$, **** $p \leq 0.0001$.

(E) Representative brightfield images of HUVECs at 0 h, 6 h, and 12 h and HUtMECs at 0 h, 12 h, and 24 h, treated with EOM or conditioned media from EOs at Post-breakdown 24 h, in a wound healing assay.

(F) Bar plots showing the normalized velocity of wound closure of HUVECs and HUtMECs treated with endothelial cell media, EOM, or conditioned media from EOs from four independent donors. Statistical analysis was performed using ordinary one-way ANOVA. *** $p \leq 0.001$, **** $p \leq 0.0001$.

tissue function.[56,57] Our findings provide a foundation for building co-culture systems, enabling a deeper understanding of how these populations interact to restore tissue integrity.

In summary, our findings establish the luminal epithelium as a central signaling hub during endometrial regeneration. We identify WNT7A as a key regulator of endometrial epithelial regeneration, opening opportunities to dissect its role in wound healing and implications for its dysregulation in endometrial pathologies.[58,59] Beyond uncovering the fundamental principles of menstrual regeneration, the IVMC protocol provides a platform to investigate how the epithelium changes during the menstrual cycle and enables studies on how menstrual cycle dynamics are perturbed in gynecological disorders, including endometriosis, Asherman syndrome, and polycystic ovary syndrome (PCOS).[29,32,60–63] Ultimately, these insights may guide new therapeutic strategies, extending their relevance beyond reproduction to fundamental processes of tissue renewal and wound healing.

Limitations of the study

There are limitations to this study. The timing of hormonal withdrawal in the IVMC protocol was aligned with our 6-day differentiation regimen. Therefore, the protocol does not fully capture the gradual hormonal decline seen *in vivo*. Further optimization of the differentiation duration and media components would be needed to increase the abundance of late secretory states. At the level of cell identity, distinguishing luminal or glandular epithelial cell states *in vitro* remains challenging due to a lack of clear markers *in vivo*. Although we detect phase-specific expression of both regeneration- and receptivity-associated luminal markers *in vivo*, this is not exclusive in all cases, as luminal markers can also be detected in glandular cells. An in-depth spatial analysis of the endometrium is necessary to more precisely define distinct markers between luminal and glandular cells. Notably, despite the lack of tissue geometry in EOs, key phase-specific expression of luminal and glandular markers is preserved.

The experimental system and setup are intentionally reductionist to enable a detailed analysis of epithelial-intrinsic regenerative programs. Incorporation of non-epithelial cell types will be an important next step toward tissue-level modeling of post-menstrual regeneration. While our data suggest signaling between epithelial-endothelial cells during regeneration, further studies are needed to explore the bidirectionality of these interactions.

Finally, while *WNT7A* emerges as a key marker of the regenerating luminal epithelium, its downstream signaling remains to be elucidated. Addressing this aspect will further strengthen mechanistic insight and enhance the translational potential of these findings.

RESOURCE AVAILABILITY

Lead contact

Requests for further information and resources should be directed to and will be fulfilled by the lead contact, Margherita Yayoi Turco, at margherita.turco@fmi.ch.

Materials availability

The transfer and use of all human endometrial tissue samples together with the established human endometrial organoid cultures for this study are authorized under material transfer agreements (MTAs) between the University of Cambridge and the Friedrich Miescher Institute for Biomedical Research (agreements nos. G119629 and G108313). The distribution of donor-derived organoid lines and endometrial tissues is subject to the ethical regulations governing the use of human biological material and the agreement stipulated in the MTA.

Data and code availability

Datasets generated for this study are available in ArrayExpress with accession numbers Array Express: E-MTAB-15118 for bulk RNA-seq data from EOs in the IVMC protocol and controls, and Array Express: E-MTAB-15330 for the scRNA-seq data from EOs in the IVMC protocol and are publicly available as of the date of publication. This study involves the re-analysis of published scRNA-seq datasets of endometrial tissue obtained from public repositories (Array Express: E-MTAB-10287, GEO: GSE111976, GEO: GSE183837, GEO: GSE214411, and GEO: GSE203191). All source code used for analysis and generation of plots is available from GitHub (https://github.com/fmicompbio/IVMC-protocol) and archived on Zenodo at https://doi.org/10.5281/zenodo.19334152 and is publicly available as of the date of publication. Raw data of the Luminex assay are deposited on Mendeley at https://doi.org/10.17632/vpmzzd54r5.1 and are publicly available as of the date of publication.

ACKNOWLEDGMENTS

We are grateful to A. Moffett, C. Tsiairis, and P. Liberali for valuable feedback on the manuscript. We are grateful to the Turco lab, particularly E. Magistrati and I. Calvi, for their support and contribution to discussions. We would also like to thank M. Huch and H. Critchley for their critical feedback on the project and D. Schübeler and H. Grosshans for their advice and support. We would like to thank the members of the Facility for Advanced Imaging and Microscopy, L. Gelman, L. Plantard, M. Bourbon, J. Eglinger, and T.-O. Buchholz for their technical support with imaging and signal quantification. We are grateful to the functional genomics facility, S. Smallwood, and S. Aluri for coordinating and performing RNA sequencing experiments. We are also thankful to our colleagues in Novartis, E. Simon and N. Stoehr, for their help with live-cell imaging of endothelial cells and the Luminex assay. We would like to thank G. J. Burton, K. Elder, and Bourn Hall Fertility Clinic for the derivation of endometrial organoid cultures. This work was supported by the Novartis Research Foundation. We thank the anonymous reviewers for their insightful feedback and constructive criticism, which significantly improved the manuscript.

AUTHOR CONTRIBUTIONS

K.N. and M.Y.T. conceived and designed experiments. K.N., W.Y., and L.K. performed experiments. K.N., C.S., and H.-R.H. analyzed data. T.C.-D. derived endometrial organoids. K.N and M.Y.T. interpreted the data. K.N. and M.Y.T. wrote the manuscript. K.N, W.Y., L.F., L.K., T.C.-D., C.S, H.-R.H., and M.Y.T. reviewed the manuscript.

DECLARATION OF INTERESTS

The authors declare no competing interests.

STAR★METHODS

Detailed methods are provided in the online version of this paper and include the following:

- KEY RESOURCES TABLE
- EXPERIMENTAL MODEL AND STUDY PARTICIPANT DETAILS
  - ○ Human endometrial tissue blocks
  - ○ Human EO lines
  - ○ Expansion and differentiation of EOs
  - ○ Primary Endothelial Cell Culture
- METHOD DETAILS
  - ○ Single cell dissociation
  - ○ Fixation and paraffin embedding of EOs
  - ○ Immunohistochemistry

Please cite this article in press as: Nikolakopoulou et al., An *in vitro* menstrual cycle using organoids captures epithelial cell transitions during menstruation and regeneration of the human endometrium, Cell Stem Cell (2026), https://doi.org/10.1016/j.stem.2026.04.005

SUPPLEMENTAL INFORMATION

Supplemental information can be found online at https://doi.org/10.1016/j.stem.2026.04.005.

Received: August 28, 2025
Revised: February 13, 2026
Accepted: April 6, 2026

REFERENCES

1. Critchley, H.O.D., Maybin, J.A., Armstrong, G.M., and Williams, A.R.W. (2020). Physiology of the endometrium and regulation of menstruation. Physiol. Rev. *100*, 1149–1179. https://doi.org/10.1152/physrev.00031.2019.
2. Emera, D., Romero, R., and Wagner, G. (2012). The evolution of menstruation: a new model for genetic assimilation: explaining molecular origins of maternal responses to fetal invasiveness. Bioessays *34*, 26–35. https://doi.org/10.1002/bies.201100099.
3. Ludwig, H., and Spornitz, U.M. (1991). Microarchitecture of the human endometrium by scanning electron microscopy: menstrual desquamation and remodeling. Ann. NY Acad. Sci. *622*, 28–46. https://doi.org/10.1111/j.1749-6632.1991.tb37848.x.
4. Padykula, H.A. (1991). Regeneration in the Primate Uterus: The Role of Stem Cells. Ann. NY Acad. Sci. *622*, 47–56. https://doi.org/10.1111/j.1749-6632.1991.tb37849.x.
5. Gaide Chevronnay, H.P., Galant, C., Lemoine, P., Courtoy, P.J., Marbaix, E., and Henriet, P. (2009). Spatiotemporal coupling of focal extracellular matrix degradation and reconstruction in the menstrual human endometrium. Endocrinology *150*, 5094–5105. https://doi.org/10.1210/en.2009-0750.
6. Garry, R., Hart, R., Karthigasu, K.A., and Burke, C. (2009). A re-appraisal of the morphological changes within the endometrium during menstruation: a hysteroscopic, histological and scanning electron microscopic study. Hum. Reprod. *24*, 1393–1401. https://doi.org/10.1093/humrep/dep036.
7. Tempest, N., Baker, A.M., Wright, N.A., and Hapangama, D.K. (2018). Does human endometrial LGR5 gene expression suggest the existence of another hormonally regulated epithelial stem cell niche? Hum. Reprod. *33*, 1052–1062. https://doi.org/10.1093/humrep/dey083.
8. Turco, M.Y., Gardner, L., Hughes, J., Cindrova-Davies, T., Gomez, M.J., Farrell, L., Hollinshead, M., Marsh, S.G.E., Brosens, J.J., Critchley, H.O., et al. (2017). Long-term, hormone-responsive organoid cultures of human endometrium in a chemically defined medium. Nat. Cell Biol. *19*, 568–577. https://doi.org/10.1038/ncb3516.
9. Garcia-Alonso, L., Handfield, L.-F., Roberts, K., Nikolakopoulou, K., Fernando, R.C., Gardner, L., Woodhams, B., Arutyunyan, A., Polanski, K., Hoo, R., et al. (2021). Mapping the temporal and spatial dynamics of the human endometrium in vivo and in vitro. Nat. Genet. *53*, 1698–1711. https://doi.org/10.1038/s41588-021-00972-2.
10. Boretto, M., Cox, B., Noben, M., Hendriks, N., Fassbender, A., Roose, H., Amant, F., Timmerman, D., Tomassetti, C., Vanhie, A., et al. (2017). Development of organoids from mouse and human endometrium showing endometrial epithelium physiology and long-term expandability. Development *144*, 1775–1786. https://doi.org/10.1242/dev.148478.
11. Salamonsen, L.A., and Woolley, D.E. (1999). Menstruation: induction by matrix metalloproteinases and inflammatory cells. J. Reprod. Immunol. *44*, 1–27. https://doi.org/10.1016/S0165-0378(99)00002-9.
12. Evans, J., and Salamonsen, L.A. (2014). Decidualized human endometrial stromal cells are sensors of hormone withdrawal in the menstrual inflammatory cascade. Biol. Reprod. *90*, 14. https://doi.org/10.1095/biolreprod.113.108175.
13. Valentijn, A.J., Palial, K., Al-Lamee, H., Tempest, N., Drury, J., Von Zglinicki, T., Saretzki, G., Murray, P., Gargett, C.E., and Hapangama, D.K. (2013). SSEA-1 isolates human endometrial basal glandular epithelial cells: phenotypic and functional characterization and implications in the pathogenesis of endometriosis. Hum. Reprod. *28*, 2695–2708. https://doi.org/10.1093/humrep/det285.
14. Nguyen, H.P.T., Xiao, L., Deane, J.A., Tan, K.-S., Cousins, F.L., Masuda, H., Sprung, C.N., Rosamilia, A., and Gargett, C.E. (2017). N-cadherin identifies human endometrial epithelial progenitor cells by in vitro stem cell assays. Hum. Reprod. *32*, 2254–2268. https://doi.org/10.1093/humrep/dex289.
15. Ma, S., Hirata, T., Arakawa, T., Sun, H., Neriishi, K., Fukuda, S., Nakazawa, A., Wang, Y., Harada, M., Hirota, Y., et al. (2020). Expression of ALDH1A Isozymes in Human Endometrium with and without Endometriosis and in Ovarian Endometrioma. Reprod. Sci. *27*, 443–452. https://doi.org/10.1007/s43032-019-00041-4.
16. Syed, S.M., Kumar, M., Ghosh, A., Tomasetig, F., Ali, A., Whan, R.M., Alterman, D., and Tanwar, P.S. (2020). Endometrial Axin2+ Cells Drive Epithelial Homeostasis, Regeneration, and Cancer following Oncogenic Transformation. Cell Stem Cell *26*, 64–80.e13. https://doi.org/10.1016/j.stem.2019.11.012.
17. Boggavarapu, N.R., Lalitkumar, S., Joshua, V., Kasvandik, S., Salumets, A., Lalitkumar, P.G., and Gemzell-Danielsson, K. (2016). Compartmentalized gene expression profiling of receptive endometrium reveals progesterone regulated ENPP3 is differentially expressed and secreted in glycosylated form. Sci. Rep. *6*, 33811. https://doi.org/10.1038/srep33811.
18. Tabibzadeh, S., Kong, Q.F., Babaknia, A., and May, L.T. (1995). Progressive rise in the expression of interleukin-6 in human endometrium during menstrual cycle is initiated during the implantation window. Hum. Reprod. *10*, 2793–2799. https://doi.org/10.1093/oxfordjournals.humrep.a135793.
19. Cullinan, E.B., Abbondanzo, S.J., Anderson, P.S., Pollard, J.W., Lessey, B.A., and Stewart, C.L. (1996). Leukemia inhibitory factor (LIF) and LIF receptor expression in human endometrium suggests a potential autocrine/paracrine function in regulating embryo implantation. Proc. Natl. Acad. Sci. USA *93*, 3115–3120. https://doi.org/10.1073/pnas.93.7.3115.
20. Burton, G.J., Watson, A.L., Hempstock, J., Skepper, J.N., and Jauniaux, E. (2002). Uterine glands provide histiotrophic nutrition for the human fetus during the first trimester of pregnancy. J. Clin. Endocrinol. Metab. *87*, 2954–2959. https://doi.org/10.1210/jcem.87.6.8563.
21. Martínez-Aguilar, R., Kershaw, L.E., Reavey, J.J., Critchley, H.O.D., and Maybin, J.A. (2021). HYPOXIA AND REPRODUCTIVE HEALTH: The presence and role of hypoxia in the endometrium. Reproduction *161*, F1–F17. https://doi.org/10.1530/REP-20-0268.
22. Naseri, S., Rosenberg-Hasson, Y., Maecker, H.T., Avrutsky, M.I., and Blumenthal, P.D. (2023). A cross-sectional study comparing the inflammatory profile of menstrual effluent vs. peripheral blood. Health Sci. Rep. *6*, e1038. https://doi.org/10.1002/hsr2.1038.
23. Nordengren, J., Pilka, R., Noskova, V., Ehinger, A., Domanski, H., Andersson, C., Høyer-Hansen, G., Hansson, S.R., and Casslén, B. (2004). Differential localization and expression of urokinase plasminogen

activator (uPA), its receptor (uPAR), and its inhibitor (PAI-1) mRNA and protein in endometrial tissue during the menstrual cycle. Mol. Hum. Reprod. *10*, 655–663. https://doi.org/10.1093/molehr/gah081.

24. Wilson, Z.S., Raya-Sandino, A., Miranda, J., Fan, S., Brazil, J.C., Quiros, M., Garcia-Hernandez, V., Liu, Q., Kim, C.H., Hankenson, K.D., et al. (2024). Critical role of thrombospondin-1 in promoting intestinal mucosal wound repair. JCI Insight *9*, e180608. https://doi.org/10.1172/jci.insight.180608.
25. Lin, B., Shah, V.S., Chernoff, C., Sun, J., Shipkovenska, G.G., Vinarsky, V., Waghray, A., Xu, J., Leduc, A.D., Hintschich, C.A., et al. (2024). Airway hillocks are injury-resistant reservoirs of unique plastic stem cells. Nature *629*, 869–877. https://doi.org/10.1038/s41586-024-07377-1.
26. Wang, W., Vilella, F., Alama, P., Moreno, I., Mignardi, M., Isakova, A., Pan, W., Simon, C., and Quake, S.R. (2020). Single-cell transcriptomic atlas of the human endometrium during the menstrual cycle. Nat. Med. *26*, 1644–1653. https://doi.org/10.1038/s41591-020-1040-z.
27. Lai, Z.-Z., Wang, Y., Zhou, W.-J., Liang, Z., Shi, J.-W., Yang, H.-L., Xie, F., Chen, W.-D., Zhu, R., Zhang, C., et al. (2022). Single-cell transcriptome profiling of the human endometrium of patients with recurrent implantation failure. Theranostics *12*, 6527–6547. https://doi.org/10.7150/thno.74053.
28. Huang, X., Wu, L., Pei, T., Liu, D., Liu, C., Luo, B., Xiao, L., Li, Y., Wang, R., Ouyang, Y., et al. (2023). Single-cell transcriptome analysis reveals endometrial immune microenvironment in minimal/mild endometriosis. Clin. Exp. Immunol. *212*, 285–295. https://doi.org/10.1093/cei/uxad029.
29. Shih, A.J., Adelson, R.P., Vashistha, H., Khalili, H., Nayyar, A., Puran, R., Herrera, R., Chatterjee, P.K., Lee, A.T., Truskinovsky, A.M., et al. (2022). Single-cell analysis of menstrual endometrial tissues defines phenotypes associated with endometriosis. BMC Med. *20*, 315. https://doi.org/10.1186/s12916-022-02500-3.
30. Marečková, M., Garcia-Alonso, L., Moullet, M., Lorenzi, V., Petryszak, R., Sancho-Serra, C., Oszlanczi, A., Icoresi Mazzeo, C., Wong, F.C.K., Kelava, I., et al. (2024). An integrated single-cell reference atlas of the human endometrium. Nat. Genet. *56*, 1925–1937. https://doi.org/10.1038/s41588-024-01873-w.
31. Young, S.L., and Lessey, B.A. (2010). Progesterone function in human endometrium: clinical perspectives. Semin. Reprod. Med. *28*, 5–16. https://doi.org/10.1055/s-0029-1242988.
32. Tan, Y., Flynn, W.F., Sivajothi, S., Luo, D., Bozal, S.B., Davé, M., Luciano, A.A., Robson, P., Luciano, D.E., and Courtois, E.T. (2022). Single-cell analysis of endometriosis reveals a coordinated transcriptional programme driving immunotolerance and angiogenesis across eutopic and ectopic tissues. Nat. Cell Biol. *24*, 1306–1318. https://doi.org/10.1038/s41556-022-00961-5.
33. Shehata, M., Teschendorff, A., Sharp, G., Novcic, N., Russell, I.A., Avril, S., Prater, M., Eirew, P., Caldas, C., Watson, C.J., et al. (2012). Phenotypic and functional characterisation of the luminal cell hierarchy of the mammary gland. Breast Cancer Res. *14*, R134. https://doi.org/10.1186/bcr3334.
34. Reed, M., Luissint, A.-C., Azcutia, V., Fan, S., O'Leary, M.N., Quiros, M., Brazil, J., Nusrat, A., and Parkos, C.A. (2019). Epithelial CD47 is critical for mucosal repair in the murine intestine in vivo. Nat. Commun. *10*, 5004. https://doi.org/10.1038/s41467-019-12968-y.
35. Fan, X., Krieg, S., Hwang, J.Y., Dhal, S., Kuo, C.J., Lasley, B.L., Brenner, R.M., and Nayak, N.R. (2012). Dynamic regulation of Wnt7a expression in the primate endometrium: implications for postmenstrual regeneration and secretory transformation. Endocrinology *153*, 1063–1069. https://doi.org/10.1210/en.2011-1826.
36. Dunlap, K.A., Filant, J., Hayashi, K., Rucker, E.B., III, Song, G., Deng, J.M., Behringer, R.R., DeMayo, F.J., Lydon, J., Jeong, J.-W., et al. (2011). Postnatal Deletion of Wnt7a Inhibits Uterine Gland Morphogenesis and Compromises Adult Fertility in Mice. Biol. Reprod. *85*, 386–396. https://doi.org/10.1095/biolreprod.111.091769.
37. Haider, S., Gamperl, M., Burkard, T.R., Kunihs, V., Kaindl, U., Junttila, S., Fiala, C., Schmidt, K., Mendjan, S., Knöfler, M., et al. (2019). Estrogen Signaling Drives Ciliogenesis in Human Endometrial Organoids. Endocrinology *160*, 2282–2297. https://doi.org/10.1210/en.2019-00314.
38. Choksi, S.P., Byrnes, L.E., Konjikusic, M.J., Tsai, B.W.H., Deleon, R., Lu, Q., Westlake, C.J., and Reiter, J.F. (2024). An alternative cell cycle coordinates multiciliated cell differentiation. Nature *630*, 214–221. https://doi.org/10.1038/s41586-024-07476-z.
39. Johnson, B.Z., Stevenson, A.W., Prêle, C.M., Fear, M.W., and Wood, F.M. (2020). The Role of IL-6 in Skin Fibrosis and Cutaneous Wound Healing. Biomedicines *8*, 101. https://doi.org/10.3390/biomedicines8050101.
40. Vilotić, A., Nacka-Aleksić, M., Pirković, A., Bojić-Trbojević, Ž., Dekanski, D., and Jovanović Krivokuća, M. (2022). IL-6 and IL-8: An Overview of Their Roles in Healthy and Pathological Pregnancies. Int. J. Mol. Sci. *23*, 14574. https://doi.org/10.3390/ijms232314574.
41. Cousins, F.L., Kirkwood, P.M., Saunders, P.T.K., and Gibson, D.A. (2016). Evidence for a dynamic role for mononuclear phagocytes during endometrial repair and remodelling. Sci. Rep. *6*, 36748. https://doi.org/10.1038/srep36748.
42. Perretti, M., and D'Acquisto, F. (2009). Annexin A1 and glucocorticoids as effectors of the resolution of inflammation. Nat. Rev. Immunol. *9*, 62–70. https://doi.org/10.1038/nri2470.
43. Cambier, S., Gouwy, M., and Proost, P. (2023). The chemokines CXCL8 and CXCL12: molecular and functional properties, role in disease and efforts towards pharmacological intervention. Cell. Mol. Immunol. *20*, 217–251. https://doi.org/10.1038/s41423-023-00974-6.
44. Maybin, J.A., Hirani, N., Jabbour, H.N., and Critchley, H.O.D. (2011). Novel roles for hypoxia and prostaglandin E2 in the regulation of IL-8 during endometrial repair. Am. J. Pathol. *178*, 1245–1256. https://doi.org/10.1016/j.ajpath.2010.11.070.
45. Miller, C., and Sassoon, D.A. (1998). Wnt-7a maintains appropriate uterine patterning during the development of the mouse female reproductive tract. Development *125*, 3201–3211. https://doi.org/10.1242/dev.125.16.3201.
46. Carta, L., and Sassoon, D. (2004). Wnt7a Is a Suppressor of Cell Death in the Female Reproductive Tract and Is Required for Postnatal and Estrogen-Mediated Growth. Biol. Reprod. *71*, 444–454. https://doi.org/10.1095/biolreprod.103.026534.
47. Le Grand, F., Jones, A.E., Seale, V., Scimè, A., and Rudnicki, M.A. (2009). Wnt7a Activates the Planar Cell Polarity Pathway to Drive the Symmetric Expansion of Satellite Stem Cells. Cell Stem Cell *4*, 535–547. https://doi.org/10.1016/j.stem.2009.03.013.
48. Alsaadi, A., Artibani, M., Hu, Z., Wietek, N., Morotti, M., Gonzalez, L.S., Alazzam, M., Jiang, J., Abdul, B., Soleymani Majd, H., et al. (2023). Single-cell transcriptomics identifies a WNT7A-FZD5 signaling axis that maintains fallopian tube stem cells in patient-derived organoids. Cell Rep. *42*, 113354. https://doi.org/10.1016/j.celrep.2023.113354.
49. Qu, Q., Sun, G., Murai, K., Ye, P., Li, W., Asuelime, G., Cheung, Y.-T., and Shi, Y. (2013). Wnt7a Regulates Multiple Steps of Neurogenesis. Mol. Cell. Biol. *33*, 2551–2559. https://doi.org/10.1128/MCB.00325-13.
50. Dong, L., Hao, H., Liu, J., Ti, D., Tong, C., Hou, Q., Li, M., Zheng, J., Liu, G., Fu, X., et al. (2017). A Conditioned Medium of Umbilical Cord Mesenchymal Stem Cells Overexpressing Wnt7a Promotes Wound Repair and Regeneration of Hair Follicles in Mice. Stem Cells Int. *2017*, 3738071. https://doi.org/10.1155/2017/3738071.
51. Lan, L., Wang, W., Huang, Y., Bu, X., and Zhao, C. (2019). Roles of Wnt7a in embryo development, tissue homeostasis, and human diseases. J. Cell. Biochem. *120*, 18588–18598. https://doi.org/10.1002/jcb.29217.
52. Gibson, A.L., Hui Mingalone, C.K., Foote, A.T., Uchimura, T., Zhang, M., and Zeng, L. (2017). Wnt7a Inhibits IL-1β Induced Catabolic Gene Expression and Prevents Articular Cartilage Damage in Experimental Osteoarthritis. Sci. Rep. *7*, 41823. https://doi.org/10.1038/srep41823.
53. Wallace, J., Lutgen, V., Avasarala, S., St Croix, B., Winn, R.A., and Al-Harthi, L. (2018). Wnt7a induces a unique phenotype of monocyte-derived macrophages with lower phagocytic capacity and differential expression

Please cite this article in press as: Nikolakopoulou et al., An *in vitro* menstrual cycle using organoids captures epithelial cell transitions during menstruation and regeneration of the human endometrium, Cell Stem Cell (2026), https://doi.org/10.1016/j.stem.2026.04.005

of pro- and anti-inflammatory cytokines. Immunology *153*, 203–213. https://doi.org/10.1111/imm.12830.

54. Carmon, K.S., and Loose, D.S. (2008). Secreted frizzled-related protein 4 regulates two Wnt7a signaling pathways and inhibits proliferation in endometrial cancer cells. Mol. Cancer Res. *6*, 1017–1028. https://doi.org/10.1158/1541-7786.MCR-08-0039.
55. Heidemann, J., Ogawa, H., Dwinell, M.B., Rafiee, P., Maaser, C., Gockel, H.R., Otterson, M.F., Ota, D.M., Lugering, N., Domschke, W., et al. (2003). Angiogenic effects of interleukin 8 (CXCL8) in human intestinal microvascular endothelial cells are mediated by CXCR2. J. Biol. Chem. *278*, 8508–8515. https://doi.org/10.1074/jbc.M208231200.
56. Gnecco, J.S., Brown, A., Buttrey, K., Ives, C., Goods, B.A., Baugh, L., Hernandez-Gordillo, V., Loring, M., Isaacson, K.B., and Griffith, L.G. (2023). Organoid co-culture model of the human endometrium in a fully synthetic extracellular matrix enables the study of epithelial-stromal crosstalk. Med *4*, 554–579.e9. https://doi.org/10.1016/j.medj.2023.07.004.
57. Rawlings, T.M., Tryfonos, M., Makwana, K., Taylor, D.M., Brosens, J.J., and Lucas, E.S. (2024). Endometrial Assembloids to Model Human Embryo Implantation In Vitro. Methods Mol. Biol. *2767*, 63–74. https://doi.org/10.1007/7651_2023_495.
58. Gurriaran-Rodriguez, U., Kodippili, K., Datzkiw, D., Javandoost, E., Xiao, F., Rejas, M.T., and Rudnicki, M.A. (2024). Wnt7a is required for regeneration of dystrophic skeletal muscle. Skelet. Muscle *14*, 34. https://doi.org/10.1186/s13395-024-00367-x.
59. Wang, W., Yan, X., Lin, Y., Ge, H., and Tan, Q. (2018). Wnt7a promotes wound healing by regulation of angiogenesis and inflammation: Issues on diabetes and obesity. J. Dermatol. Sci. *91*. S0923-1811(18)30103-8. https://doi.org/10.1016/j.jdermsci.2018.02.007.
60. Liu, S., Li, X., Gu, Z., Wu, J., Jia, S., Shi, J., Dai, Y., Wu, Y., Yan, H., Zhang, J., et al. (2025). Single-cell and spatial transcriptomic profiling revealed niche interactions sustaining growth of endometriotic lesions. Cell Genomics *5*, 100737. https://doi.org/10.1016/j.xgen.2024.100737.
61. Fonseca, M.A.S., Haro, M., Wright, K.N., Lin, X., Abbasi, F., Sun, J., Hernandez, L., Orr, N.L., Hong, J., Choi-Kuaea, Y., et al. (2023). Single-cell transcriptomic analysis of endometriosis. Nat. Genet. *55*, 255–267. https://doi.org/10.1038/s41588-022-01254-1.
62. Santamaria, X., Roson, B., Perez-Moraga, R., Venkatesan, N., Pardo-Figuerez, M., Gonzalez-Fernandez, J., Llera-Oyola, J., Fernández, E., Moreno, I., Salumets, A., et al. (2023). Decoding the endometrial niche of Asherman's Syndrome at single-cell resolution. Nat. Commun. *14*, 5890. https://doi.org/10.1038/s41467-023-41656-1.
63. Eriksson, G., Li, C., Sparovec, T.G., Dekanski, A., Torstensson, S., Risal, S., Ohlsson, C., Hirschberg, A.L., Petropoulos, S., Deng, Q., et al. (2025). Single-cell profiling of the human endometrium in polycystic ovary syndrome. Nat. Med. *31*, 1925–1938. https://doi.org/10.1038/s41591-025-03592-z.
64. Mudge, J.M., Carbonell-Sala, S., Diekhans, M., Martinez, J.G., Hunt, T., Jungreis, I., Loveland, J.E., Arnan, C., Barnes, I., Bennett, R., et al. (2025). GENCODE 2025: reference gene annotation for human and mouse. Nucleic Acids Res. *53*, D966–D975. https://doi.org/10.1093/nar/gkae1078.
65. Robinson, M.D., McCarthy, D.J., and Smyth, G.K. (2010). edgeR: a Bioconductor package for differential expression analysis of digital gene expression data. Bioinformatics *26*, 139–140. https://doi.org/10.1093/bioinformatics/btp616.
66. Patro, R., Duggal, G., Love, M.I., Irizarry, R.A., and Kingsford, C. (2017). Salmon provides fast and bias-aware quantification of transcript expression. Nat. Methods *14*, 417–419. https://doi.org/10.1038/nmeth.4197.
67. He, D., Zakeri, M., Sarkar, H., Soneson, C., Srivastava, A., and Patro, R. (2022). Alevin-fry unlocks rapid, accurate and memory-frugal quantification of single-cell RNA-seq data. Nat. Methods *19*, 316–322. https://doi.org/10.1038/s41592-022-01408-3.
68. McCarthy, D.J., Campbell, K.R., Lun, A.T.L., and Wills, Q.F. (2017). Scater: pre-processing, quality control, normalization and visualization of single-cell RNA-seq data in R. Bioinformatics *33*, 1179–1186. https://doi.org/10.1093/bioinformatics/btw777.
69. Haghverdi, L., Lun, A.T.L., Morgan, M.D., and Marioni, J.C. (2018). Batch effects in single-cell RNA-sequencing data are corrected by matching mutual nearest neighbors. Nat. Biotechnol. *36*, 421–427. https://doi.org/10.1038/nbt.4091.
70. Hao, Y., Stuart, T., Kowalski, M.H., Choudhary, S., Hoffman, P., Hartman, A., Srivastava, A., Molla, G., Madad, S., Fernandez-Granda, C., et al. (2024). Dictionary learning for integrative, multimodal and scalable single-cell analysis. Nat. Biotechnol. *42*, 293–304. https://doi.org/10.1038/s41587-023-01767-y.
71. Melville, J., Lun, A., Djekidel, M.N., Hao, Y., Eddelbuettel, D., and Bijl, W. van der. (2025). uwot: The Uniform Manifold Approximation and Projection (UMAP) Method for Dimensionality Reduction, [Version 0.2.3].
72. Chu, T., Wang, Z., Pe'er, D., and Danko, C.G. (2022). Cell type and gene expression deconvolution with BayesPrism enables Bayesian integrative analysis across bulk and single-cell RNA sequencing in oncology. Nat. Cancer *3*, 505–517. https://doi.org/10.1038/s43018-022-00356-3.
73. Aran, D., Looney, A.P., Liu, L., Wu, E., Fong, V., Hsu, A., Chak, S., Naikawadi, R.P., Wolters, P.J., Abate, A.R., et al. (2019). Reference-based analysis of lung single-cell sequencing reveals a transitional profibrotic macrophage. Nat. Immunol. *20*, 163–172. https://doi.org/10.1038/s41590-018-0276-y.
74. Jin, S., Guerrero-Juarez, C.F., Zhang, L., Chang, I., Ramos, R., Kuan, C.-H., Myung, P., Plikus, M.V., and Nie, Q. (2021). Inference and analysis of cell-cell communication using CellChat. Nat. Commun. *12*, 1088. https://doi.org/10.1038/s41467-021-21246-9.
75. Srivastava, A., Malik, L., Sarkar, H., Zakeri, M., Almodaresi, F., Soneson, C., Love, M.I., Kingsford, C., and Patro, R. (2020). Alignment and mapping methodology influence transcript abundance estimation. Genome Biol. *21*, 239. https://doi.org/10.1186/s13059-020-02151-8.
76. Love, M.I., Soneson, C., Hickey, P.F., Johnson, L.K., Pierce, N.T., Shepherd, L., Morgan, M., and Patro, R. (2020). Tximeta: Reference sequence checksums for provenance identification in RNA-seq. PLOS Comput. Biol. *16*, e1007664. https://doi.org/10.1371/journal.pcbi.1007664.
77. zellkonverter Bioconductor. http://bioconductor.org/packages/zellkonverter/. Bioconductor.
78. Index of /Pub/Databases/Gencode/Gencode_human/release_38 https://ftp.ebi.ac.uk/pub/databases/gencode/Gencode_human/release_38/.
79. Soneson, C., Srivastava, A., Patro, R., and Stadler, M.B. (2021). Preprocessing choices affect RNA velocity results for droplet scRNA-seq data. PLOS Comput. Biol. *17*, e1008585. https://doi.org/10.1371/journal.pcbi.1008585.
80. Lawrence, M., Huber, W., Pagès, H., Aboyoun, P., Carlson, M., Gentleman, R., Morgan, M.T., and Carey, V.J. (2013). Software for Computing and Annotating Genomic Ranges. PLOS Comput. Biol. *9*, e1003118. https://doi.org/10.1371/journal.pcbi.1003118.
81. alevinQC Bioconductor. http://bioconductor.org/packages/alevinQC/. Bioconductor.
82. Zhu, A., Srivastava, A., Ibrahim, J.G., Patro, R., and Love, M.I. (2019). Nonparametric expression analysis using inferential replicate counts. Nucleic Acids Res. *47*, e105. https://doi.org/10.1093/nar/gkz622.
83. Lun, A.T.L., McCarthy, D.J., and Marioni, J.C. (2016). A step-by-step workflow for low-level analysis of single-cell RNA-seq data with Bioconductor. F1000Res *5*, 2122. https://doi.org/10.12688/f1000research.9501.2.
84. McInnes, L., Healy, J., Saul, N., and Großberger, L. (2018). UMAP: Uniform Manifold Approximation and Projection. J. Open Source Softw. *3*, 861. https://doi.org/10.21105/joss.00861.
85. bluster Bioconductor. http://bioconductor.org/packages/bluster/. Bioconductor.

Please cite this article in press as: Nikolakopoulou et al., An *in vitro* menstrual cycle using organoids captures epithelial cell transitions during menstruation and regeneration of the human endometrium, Cell Stem Cell (2026), https://doi.org/10.1016/j.stem.2026.04.005

86. Csárdi, G., and Nepusz, T. (2006). The igraph software package for complex network research. In.

87. Hie, B., Cho, H., DeMeo, B., Bryson, B., and Berger, B. (2019). Geometric Sketching Compactly Summarizes the Single-Cell Transcriptomic Landscape. Cell Syst. *8*, 483–493.e7. https://doi.org/10.1016/j.cels.2019.05.003.

88. sketchR Bioconductor. http://bioconductor.org/packages/sketchR/. Bioconductor.

89. Maaten, L. van der, and Hinton, G. (2008). Visualizing Data using t-SNE. J. Mach. Learn. Res. *9*, 2579–2605.

90. Linderman, G.C., Rachh, M., Hoskins, J.G., Steinerberger, S., and Kluger, Y. (2019). Fast interpolation-based t-SNE for improved visualization of single-cell RNA-seq data. Nat. Methods *16*, 243–245. https://doi.org/10.1038/s41592-018-0308-4.

91. Traag, V.A., Waltman, L., and van Eck, N.J. (2019). From Louvain to Leiden: guaranteeing well-connected communities. Sci. Rep. *9*, 5233. https://doi.org/10.1038/s41598-019-41695-z.

92. Kolberg, L., Raudvere, U., Kuzmin, I., Vilo, J., and Peterson, H. (2020). gprofiler2 – an R package for gene list functional enrichment analysis and namespace conversion toolset g:Profiler. F1000Res *9*. ELIXIR-709. https://doi.org/10.12688/f1000research.24956.2.

93. Zheng, S.C., Stein-O'Brien, G., Augustin, J.J., Slosberg, J., Carosso, G.A., Winer, B., Shin, G., Bjornsson, H.T., Goff, L.A., and Hansen, K.D. (2022). Universal prediction of cell-cycle position using transfer learning. Genome Biol. *23*, 41. https://doi.org/10.1186/s13059-021-02581-y.

94. Suarez-Arnedo, A., Torres Figueroa, F.T., Clavijo, C., Arbeláez, P., Cruz, J.C., and Muñoz-Camargo, C. (2020). An Image J plugin for the high throughput image analysis of in vitro scratch wound healing assays. PLOS One *15*, e0232565. https://doi.org/10.1371/journal.pone.0232565.

Please cite this article in press as: Nikolakopoulou et al., An *in vitro* menstrual cycle using organoids captures epithelial cell transitions during menstruation and regeneration of the human endometrium, Cell Stem Cell (2026), https://doi.org/10.1016/j.stem.2026.04.005

STAR★METHODS

KEY RESOURCES TABLE

REAGENT or RESOURCE	SOURCE	IDENTIFIER
Antibodies		
Atypical Chemokine Receptor 1 (ACKR1) Rabbit Polyclonal Antibody	Atlas Antibodies	(Atlas Antibodies, Cat# HPA017672, RRID: AB_1849221)
Aldehyde Dehydrogenase 1 Family, Member A1 (ALDH1A1) Rabbit Monoclonal Antibody [D9J7R]	Cell Signaling Technology	(Cell Signaling Technology Cat# 36671; RRID: AB_2736855)
Annexin A1 Rabbit Monoclonal Antibody [D5V2T]	Cell Signaling Technology	(Cell Signaling Technology Cat# 32934; RRID: AB_2799031)
CD47 Rabbit Monoclonal Antibody [EPR21794]	Abcam	(Abcam Cat# ab218810; RRID: AB_3083705)
CK13 Rabbit Polyclonal Antibody	Abcam	(Abcam Cat# ab92551; RRID: AB_2134681)
CXCR1 (C-Terminus) Rabbit Polyclonal Antibody	LSBio	(LSBio, Cat# LS-A808)
ENPP3 Rabbit Polyclonal Antibody	Atlas Antibodies	(Atlas Antibodies Cat# HPA043772; RRID:AB_10795616)
ITGA2 Rabbit Monoclonal Antibody [7O9H6]	Novus	(Novus Cat# NBP3-15644, RRID; AB_3598772)
Ki-67 Recombinant Rabbit Monoclonal Antibody [SP6]	Thermo Fisher Scientific	(Thermo Fisher Scientific Cat# MA5-14520; RRID: AB_10979488)
PAEP Rabbit Monoclonal Antibody [EPR23251-87]	Abcam	(Abcam Cat# ab270454)
PGR Rabbit Monoclonal Antibody [D8Q2J]	Cell Signaling Technology	(Cell Signaling Technology Cat# 8757; RRID: AB_2797144)
SOX9 Rabbit Monoclonal Antibody [EPR14335]	Abcam	(Abcam Cat# ab185230; RRID: AB_2715497)
SSEA1 Rabbit Monoclonal Antibody [1478R]	Abcam	(Abcam Cat# ab218403)
THBS1 Rabbit Monoclonal Antibody [R06-5F3]	Thermo Fisher Scientific	(Thermo Fisher Scientific Cat# RAB01344; RRID: AB_3709914)
uPA Receptor/U-PAR Rabbit Monoclonal Antibody [EPR20191]	Abcam	(Abcam Cat# ab218106; RRID: AB_3676259)
VIMENTIN Rabbit Monoclonal Antibody [D21H3]	Cell Signaling Technology	(Cell Signaling Technology Cat# 5741)
WNT7A Rabbit Monoclonal Antibody [EPR23471-125]	Abcam	(Abcam Cat# ab274321)
Biological samples		
Primary endometrial organoids (EOs)_ B003	Bourn Hall Fertility Clinic, Cambridge, UK	Endometrial biopsy donor B003
Primary endometrial organoids (EOs)_ B032	Bourn Hall Fertility Clinic, Cambridge, UK	Endometrial biopsy donor B032
Primary endometrial organoids (EOs)_ B044	Bourn Hall Fertility Clinic, Cambridge, UK	Endometrial biopsy donor B044
Primary endometrial organoids (EOs)_ B050	Bourn Hall Fertility Clinic, Cambridge, UK	Endometrial biopsy donor B050
Primary endometrial organoids (EOs)_ B066	Bourn Hall Fertility Clinic, Cambridge, UK	Endometrial biopsy donor B066
Primary endometrial organoids (EOs)_ B078	Bourn Hall Fertility Clinic, Cambridge, UK	Endometrial biopsy donor B078
Primary endometrial organoids (EOs)_ B080	Bourn Hall Fertility Clinic, Cambridge, UK	Endometrial biopsy donor B080
Chemicals, peptides, and recombinant proteins		
Advanced DMEM/F12	Life Technologies	12634010
Endothelial Cell Growth Medium MV kit	PromoCell	C-22120
ALK-4, -5, -7 inhibitor, A83-01	System Biosciences	ZRD-A8-02
B27	Life Technologies	12587010
L-glutamine	Life Technologies	25030-024

(*Continued on next page*)

Continued

REAGENT or RESOURCE	SOURCE	IDENTIFIER
N2	Life Technologies	17502048
N-Acetyl-L-cysteine	Sigma-Aldrich	A9165-5G
Nicotinamide	Sigma-Aldrich	N0636
Primocin	Invivogen	ant-pm-1
Recombinant human EGF	Peprotech	AF-100-15
Recombinant human FGF-10	Peprotech	100–26
Recombinant human HGF	Peprotech	100–39
Recombinant human Noggin	Peprotech	120-10c
Recombinant human Rspondin-1	Peprotech	120–38
Recombinant human bFGF	Peprotech	100-18B
CHIR99021	Tocris	4423
Y-27632	Millipore	688000
β-estradiol (E2)	Sigma	E4389
Progesterone (P4)	Sigma	P7556
Prolactin (PRL)	Peprotech	100-07
8-Bromoadenosine 3′, 5′-cyclic monophosphate (cAMP)	Sigma	B7880
Cell Recovery Solution	Corning	354253
Accutase cell detachment solution	Gibco	A11105-01
Collagenase V	Sigma-Aldrich	C-9263
Alt-R® S.p. HiFi Cas9 Nuclease V3	IDT Lubioscience	1081060
Cell Detach kit (for endothelial cells)	PromoCell	C-41200
Matrigel	Corning	356231
1× Halt Protease Cocktail Inhibitor	Thermo Fisher Scientific	1862209
Critical commercial assays		
RNA scope high-definition brown assay	ACD	322310
Multiplex Fluorescent V2 Assay	ACD	323100
AMAXA P3 Primary Cell 4D-NucleofectorTM X Kit S	Lonza Bioscience	V4XP-3032
SuperScript VILO cDNA Synthesis Kit	Thermo Fisher Scientific	11754050
TaqMan Fast Advanced Master Mix	Thermo Fisher Scientific	4444557
Pierce BCA Protein Assay Kit	Thermo Fisher Scientific	23225
46-plex Human Luminex Performance Assay	R&D Systems	LKTM014B
Deposited data		
Bulk RNAseq data from EOs in the IVMC protocol and controls (generated in this study)	Array Express	[Array Express]: [E-MTAB-15118]
scRNAseq data from EOs in the IVMC protocol (generated in this study)	Array Express	[Array Express]: [E-MTAB-15330]
scRNAseq data	Garcia-Alonso et al.[9]	[Array Express]: [E-MTAB-10287]
scRNAseq data	Wang et al.[26]	[GEO]: [GSE111976]
scRNAseq data	Lai et al.[27]	[GEO]: [GSE183837]
scRNAseq data	Huang et al.[28]	[GEO]: [GSE214411]
scRNAseq data	Shih et al.[29]	[GEO]: [GSE203191]
Human reference genome GENCODE release	Mudge et al.[64]	Genome Reference Consortium
Raw data from Luminex assay (all 46 analytes) (generated in this study)	Mendeley	[Mendeley] : [10.17632/vpmzzd54r5.]
Experimental models: Cell lines		
Human Uterine Microvascular Endothelial Cells (HUtMECs)	PromoCell	C-12295
Human Umbilical Vein Endothelial Cells (HUVECs)	Lonza	kindly donated by N. Gjorevski, IHB, Roche

(*Continued on next page*)

Please cite this article in press as: Nikolakopoulou et al., An *in vitro* menstrual cycle using organoids captures epithelial cell transitions during menstruation and regeneration of the human endometrium, Cell Stem Cell (2026), https://doi.org/10.1016/j.stem.2026.04.005

Continued

REAGENT or RESOURCE	SOURCE	IDENTIFIER
Oligonucleotides		
WNT7A sgRNA KO kit sgRNA (1) AGAGCGCACCGUCUUCGGGA	Synthego	N/A
WNT7A sgRNA KO kit sgRNA (2) ACUGAAACUGACACUCGUCC	Synthego	N/A
WNT7A sgRNA KO kit sgRNA (3) UGGCAGAUCGCCCGCUGUCU	Synthego	N/A
HDR Donor oligo (non-specific template) CGT GCT GCT TCA TGT GGT CGG CGG GGT AG	IDT	1274 5417
Software and algorithms		
ImageJ (version 1.54f)	Schneider et al.	https://imagej.nih.gov/ij/
edgeR version (4.6.2)	Robinson et al.[65]	https://bioconductor.org/packages/edgeR/
Salmon (v1.6.0)	Patro et al.[66]	https://salmon.readthedocs.io/en/latest/
alevin-fry (v0.4.3)	He et al.[67]	https://alevin-fry.readthedocs.io/en/latest/
alevinQC R package (v1.18.1)	Bioconductor	https://bioconductor.org/packages/alevinQC/
scuttle R package (v1.16.0)	McCarthy et al.[68]	https://bioconductor.org/packages/scuttle/
batchelor R package (v1.22.0)	Haghverdi et al.[69]	https://bioconductor.org/packages/batchelor
scater R package (v1.34.0)	McCarthy et al.[68]	https://bioconductor.org/packages/scater/
Seurat (v5.2.1)	Hao et al.[70]	https://satijalab.org/seurat/
sketchR R package (v1.2.0)	Bioconductor	http://bioconductor.org/packages/sketchR/
uwot R package (v0.2.2)	Melville et al.[71]	https://doi.org/10.32614/CRAN.package.uwot
BayesPrism package (v2.2.2)	Chu et al.[72]	https://github.com/Danko-Lab/BayesPrism
SingleR R package (v2.8.0)	Aran et al.[73]	https://bioconductor.org/packages/SingleR/
CellChat (v1.6.1)	Jin et al.[74]	https://github.com/jinworks/CellChat
GraphPad Prism 10	N/A	https://www.graphpad.com/
Other		
Source code used for analysis and generation of plots	Github https://github.com/fmicompbio/IVMC-protocol	[Zenodo] : [https://doi.org/10.5281/zenodo.19334152]

EXPERIMENTAL MODEL AND STUDY PARTICIPANT DETAILS

Human endometrial tissue blocks

Human endometrial tissue blocks were kindly donated by Professor Ashley Moffett (University of Cambridge, UK). They were collected at Addenbrookes Hospital, Cambridge before 1 September 2006 (prior to the implementation of the Human Tissue Act) and therefore formal consent for research use was not required. These samples are categorized as ‘Existing Holdings’ under the Human Tissue Act and were therefore eligible for use in this project. The hysterectomy uteri span all phases of the menstrual cycle (dated by a pathologist) and are properly oriented to allow evaluation the full thickness of the endometrium.

Human EO lines

Endometrial organoids were derived from biopsies of women in the secretory phase of the cycle undergoing IVF at the Bourn Hall Fertility Clinic with approval from East of England Cambridge Central Research Ethics Committee (17/EE/01551 IRAS 225205). The organoids used for this study were derived from women undergoing IVF for male factor infertility, who did not report gynecological disorders, and are therefore designated as normal (Table S1). The use of these materials for this study is authorized under Material Transfer Agreements (MTA) between the University of Cambridge and the Friedrich Miescher Institute for Biomedical Research (Agreements No. G119629 and G108313).

Expansion and differentiation of EOs

EOs were grown as previously described.[8] Briefly, EOs were grown in Matrigel (Corning, 356231) droplets supplemented with endometrial organoid medium (EOM) (Table S2). First, EOs were primed with 0.5 nM E2 for two days followed by four additional days of combination of 0.5 nM E2, 80 nM P4, 100 μg/mL cAMP and 20 ng/ mL PRL (Table S2). For the IVMC protocol, hormones were withdrawn the following two days with EOM being changed every 24 hours. After hormonal withdrawal, EOs were broken mechanically with automatic (300 times) and manual (100 times) pipetting. EOs were then left to grow in the absence of hormones. Another round of E2 treatment was then re-initiated for two days.

Please cite this article in press as: Nikolakopoulou et al., An *in vitro* menstrual cycle using organoids captures epithelial cell transitions during menstruation and regeneration of the human endometrium, Cell Stem Cell (2026), https://doi.org/10.1016/j.stem.2026.04.005

Primary Endothelial Cell Culture

Human Uterine Microvascular Endothelial Cells (HUtMECs) (PromoCell, C-12295) were maintained in Endothelial Cell Growth Medium MV containing Endothelial Cell Basal Medium supplemented with 2% Fetal Calf Serum, 0.004 mL/ mL Endothelial Cell Growth Supplement, 10 ng/ mL human recombinant EGF, 90 μg/ mL Heparin, 1 μg/mL Hydrocortisone (PromoCell, C-22120). Human Umbilical Vein Endothelial Cells (HUVECs) (edited to express GFP, kindly donated by N. Gjorevski, IHB, Roche) were maintained in Endothelial Cell Growth Medium containing Endothelial Cell Basal Medium supplemented with 2% Fetal Calf Serum, 0.004 mL /mL Endothelial Cell Growth Supplement, 0.1 ng/mL human recombinant EGF (adjusted concentration for HUVECs), 90 μg/mL Heparin, 1 μg/mL Hydrocortisone (PromoCell, C-22120) and 1 ng/mL human recombinant bFGF (Peprotech, 100-18B). Cells were cultured at 37 °C in a humidified incubator with 5% CO_2. Cell detachment for subculturing and seeding for wound healing assay was performed with the DetachKit (PromoCell, C-41200) containing HEPES buffered Balanced Salt Solution, 0.04%/0.03% Trypsin/EDTA Solution and Trypsin Neutralizing Solution following manufacturer's instructions.

METHOD DETAILS

Single cell dissociation

EOs were collected and Matrigel was removed using Cell Recovery Solution (Corning, 354253) for 50 min maximum on ice. EOs were washed with cold PBS pH (7.4) (Gibco, 10010-015) and broken apart by automatic pipetting (400 times). EOs were, first incubated with pre-warmed accutase cell detachment solution (Gibco, A11105-01) for 5 minutes at 37°C and next incubated with collagenase V (Sigma-Aldrich, C-9263) diluted in 10% FBS/Advanced DMEM/F12 for 20 minutes at 37°C. The digest was passed through a 40 μm nylon mesh cell strainer to ensure single cell suspension, and the flow through was collected in Falcon round bottom tubes (Corning, 352235). If undigested organoid fragments were still present, the collagenase step was repeated. Cell pellets were diluted in EOM, and cells were counted using the NucleoCounter® NC-202™ Automated Cell Counter (Chemometec, NC-200). EOs growing from single cells were supplemented with 10μM Y-27632 (Table S2) until the formation of cystic structures.

Fixation and paraffin embedding of EOs

EOs were collected at different timepoints through the IVMC. Matrigel was removed using Cell Recovery Solution (Corning, 354253) for maximum 40 min on ice. EOs were washed with cold PBS pH (7.4) (Gibco, 10010-015) and fixed in 10% neutral buffered formalin solution (Sigma-Aldrich, HT5011) for 1h at RT. Fixed EOs were centrifuged at 300 rcf, washed twice in PBS and embedded in pre-warmed, liquid Histogel (Epredia, HG-4000-012). After solidification at RT, the Histogel dome containing EOs was transferred into a labelled histology cassette (Cell Path, EAM-0309-72B) and stored in 70% ethanol until dehydration and paraffin embedding. EOs were loaded in the retort of the HistoCore PEARL tissue processor (Leica, 14 0493 50667) using overnight standard tissue dehydration method until paraffin inclusion. The samples were then removed from the tissue processor, transferred in molten paraffin and attached to the cassettes using the HistoCore Arcadia Embedding Center (Leica, 14 0393 57262 and 14 0393 57257). After solidification of the paraffin blocks, microtome (Leica, 149MULTI0C1) sectioning was performed.

Immunohistochemistry

Immunohistochemistry was performed on 3-μm-thick paraffin sections of both endometrial tissues and organoids using the Leica Bond RX automated stainer. As part of the automated staining, the sections were first deparaffinized with the BOND Dewax Solution (Biosystems Switzerland AG, AR9222) and cleared with 100% ethanol. Next, heat induced epitope retrieval was performed with BOND Epitope Retrieval Solution 1, pH6 (Biosystems Switzerland AG, AR9961) or BOND Epitope Retrieval Solution 2, pH9 (Biosystems Switzerland AG, AR9640) at 100°C for 10 to 20min depending on the primary antibody (Table S3). Sections were incubated with appropriate primary antibody dilutions for 60 minutes at room temperature followed by washes with BOND Wash Solution 1X (BOND Wash Solution 10X Concentrate, Biosystems Switzerland AG, AR9590) (Table S3). The binding sites of the primary antibodies were then revealed using the ready-to-use Bond Polymer Refine detection kit (Biosystems Switzerland AG, DS9800) containing peroxide block solution, post primary, polymer reagent, DAB chromogen and hematoxylin counterstain. Sections were then, dehydrated with consecutive 5-minute incubations in 70% ethanol, 95% ethanol and 100% ethanol. Last, sections were dried at room temperature prior to addition of Tissue-Tek® Glas™ Mounting Medium (Sakura, 1408N). Coverslips 24x50mm #1,5 (Epredia, BB02400500SC13MNZ0) were applied using Tissue-Tek® Glas™ g2-E2 instrument (Sakura). Stained sections were imaged with the Zeiss Axioscan Z1 slide scanner.

In situ hybridization assays

In situ hybridization assays were performed on 5-μm-thick paraffin sections of endometrial tissues using the RNA scope high-definition brown assay (ACD, 322310) and sections of EOs using the RNA scope Multiplex Fluorescent V2 Assay (ACD, 323100), following the manufacturer's instructions. For both assays, sections were first baked at 60 °C for 1 hour and dewaxed with xylene (Sigma-Aldrich, 534056), cleared in 100% ethanol and air-dried. The sections were then treated according to the standard protocol: 10 minutes in Hydrogen Peroxide, 15 minutes (tissue) or 10 minutes (organoids) in Target Retrieval reagent and 30 min (tissue) or 10 minutes (organoids) at 40°C in Protease Plus. Sections were then incubated with gene specific probes, including *WNT7A* (ACD, 408231), *LGR5* (ACD, 311021), *FZD6* (ACD, 460541-C2), *FZD10* (ACD, 477131-C3), for 2 hours at 40 °C and signal was amplified with appropriate kit reagents. After signal amplification, tissue and organoid sections were processed differently according to the

Please cite this article in press as: Nikolakopoulou et al., An *in vitro* menstrual cycle using organoids captures epithelial cell transitions during menstruation and regeneration of the human endometrium, Cell Stem Cell (2026), https://doi.org/10.1016/j.stem.2026.04.005

assay requirements. Tissue sections were treated with DAB for 10 min for signal visualization. Sections were then dehydrated, mounted in histological mounting media Histomount (HS-103, National Diagnostics) and imaged using the EVOS™ M5000 Imaging System (Thermo Fisher, AMF5000). After signal amplification, organoid sections were first fluorescently labelled for each probe using fluorophores; TSA Vivid 520 (ACD, 323271), TSA Vivid 650 (ACD, 323273) or TSA Plus Cyanine 3 (Akoya Biosciences, NEL744001KT) conjugated to the appropriate channel-specific amplifiers (C1/C2/C3). Sections were counterstained with DAPI (10 sec) and mounted with ProLong™ Gold Antifade Mountant (Life Technologies, P36934). Fluorescent signals were imaged using Stellaris 5 confocal microscope.

Quantification of *WNT7A* transcripts

WNT7A transcripts from *in situ* hybridization assay were quantified in ImageJ (version 1.54f) by performing spot detection using the TrackMate plugin. DoG detector parameters were set to 0.852 micron for estimated object diameter and 1000 for the quality threshold. Simple LAP tracker was applied before spot quantification. Nuclei were segmented using the StarDist 2D plugin following default settings to be used for normalization. The number of spots was then normalized to the number of nuclei. In total, 14 image scans were used from EOs at Hormonal Withdrawal 48h and Post-breakdown 24h respectively.

Illumina stranded mRNA-seq library preparation, bulk RNA-sequencing and analysis

cDNA libraries were prepared using the Illumina Stranded mRNA-Seq (Illumina IDT DNA/RNA UDI) preparation kit according to the manufacturer's instructions. Libraries were pooled and sequenced with the Illumina NovaSeq 6000 platform, producing paired end reads of 50 base pairs each (2x50bp). Demultiplexing and FASTQ file generation were performed using Illumina's bcl2fastq2 software. RNA-seq data was quantified on the transcript level using Salmon version (1.6.0)[66] with parameters –gcBias –seqBias –numGibbsSamples=50. The reference index was constructed based on the transcriptome (transcripts.fa) from GENCODE release 38[64] using the genome sequence as a decoy[75] and a k-mer length of 23. Transcript-level estimated counts from Salmon were imported into R and summarized to the gene level using tximeta version (1.16.1).[76] Raw count data were filtered to remove lowly expressed genes setting the following parameters: mincpm <- 1 and minsamples <- x, where x is the number of different donors (endometrial organoid lines) of each dataset that was analysed. The filtered dataset was normalized using the TMM (Trimmed Mean of M-values) method with the calcNormFactors function in edgeR version (4.6.2)[65] to account for differences in library size and composition. A generalized linear model (GLM) framework was used to model gene expression while accounting for donor effects. A design matrix was constructed as follows: $design \sim donor + group$ where "donor" accounts for individual variability and "group" represents the experimental conditions. DEA was performed using the quasi-likelihood F-test (QLF test). The glmQLFit function was used to fit the model, and the glmQLFTest function was applied with a contrast matrix to compare experimental conditions. Genes were classified as significantly upregulated or downregulated based on the following threshold: FDR < 0.05 and $|\log FC| > 2$ unless stated otherwise in figure legends. Data visualizations and all plots were generated using R version 4.5.0.

Public scRNA-seq data

Processed data from the Reproductive Cell Atlas was downloaded from https://www.reproductivecellatlas.org/ and converted from h5ad to SingleCellExperiment format using the zellkonverter R package (v1.12.0).[77] Cell-level annotations were extracted from the SingleCellExperiment object and incorporated into the analysis by matching cell barcodes. Cell cycle marker genes were obtained from https://github.com/ventolab/HECA-Human-Endometrial-Cell-Atlas/tree/main/utils.

scRNA-seq reference index generation

The human genome sequence (GRCh38.primary_assembly.genome.fa) and transcript annotation (gencode.v38.annotation.gtf) files were downloaded from GENCODE release 38.[78] Coordinates for transcripts and introns were extracted from the gtf file using the getFeatureRanges function from the eisaR R package (v1.6.0),[79] with arguments featureType = c("spliced", "intron"), intronType = "separate", flankLength = 50, 85 or 145 (depending on the read length), joinOverlappingIntrons = TRUE, collapseIntronsByGene = TRUE, keepIntronInFeature = TRUE. Sequences for the extracted features were obtained using the extractTranscriptSeqs function from the GenomicFeatures package (v1.46.1),[80] and a splici index[67] was generated using Salmon (v1.6.0)[66] with the k-mer length set to 23 or 31, again depending on the read length. A feature-to-gene map was created using the getTx2Gene function from the eisaR package, adding an extra column indicating the feature type (spliced or unspliced).

scRNA-seq processing (*in vivo* atlas)

Public scRNA-seq data were quantified using Salmon (v1.6.0) and alevin-fry (v0.4.3),[67] in USA (unspliced-spliced-ambiguous) mode. Alevin-fry was run with parameters '-d fw –knee-distance' (for the generate-permit-list subcommand) and '–resolution cr-like –use-mtx' (for the quant subcommand). Initial quality control was performed using the alevinQC R package (v1.18.1).[81]

Alevin-fry counts were imported into R (v4.4.2) using the loadFry function from the fishpond package (v2.12.0).[82] Spliced and ambiguous counts were added up to form the main count matrix for downstream analysis.

To select only epithelial cells for further analysis, the raw counts were normalized using size factors calculated using the computeLibraryFactors function from the scuttle R package (v1.16.0)[68] and the multiBatchNorm function from the batchelor R package (v1.22.0),[69] using the donor as the batch variable. The top 3,000 highly variable genes were defined using the modelGeneVar and getTopHVGs functions from the scran R package (v1.34.0),[83] blocking on the data set in the variance calculation, and batch correction was performed using the fastMNN implementation from batchelor, again using the donor as the batch variable. Uniform Manifold Approximation and Projection (UMAP)[84] was applied to the fastMNN reduced dimension output using the runUMAP function from the scater R package (v1.34.0),[68] and a low-resolution clustering was applied to the UMAP representation using the makeSNNgraph function from the bluster R package (v1.16.0)[85] and the cluster_louvain function from the igraph R package (v2.1.4)[86] with the resolution parameter set to 0.001. The cluster with the largest over-representation of cells from the epithelial lineage, as determined by the Human Endometrial Cell Atlas (HECA) annotations, was retained for further analysis (n=85,354 cells).

After subsetting to epithelial cells, only genes annotated as one of protein_coding (excluding ribosomal proteins, defined by the GO term "structural constituent of ribosome" (GO:0003735)), IG_V_gene, IG_C_gene, IG_J_gene, TR_C_gene, TR_J_gene, TR_V_gene, TR_D_gene, IG_D_gene, Mt_tRNA, Mt_rRNA were retained, leaving 20,231 of the original 60,649 genes. Quality metrics for cells, including the total number of UMI counts, the number of detected genes, and the fraction of the total UMI counts coming from mitochondrial genes, were calculated using the addPerCellQC function from scuttle. Further, the intronic fraction (unspliced UMI count / total UMI count) was calculated for each cell. Cells with total UMI count above 1,000, more than 500 detected genes, and mitochondrial count fraction below 25% were retained. In addition, samples with less than 30 cells remaining after these filtering steps were excluded, leaving 49,504 cells from 26 samples for further analyses.

Size factors were calculated using the computeSumFactors function from scran followed by multiBatchNorm from batchelor, using the donor as the batch annotation. 582 cells with size factors below 0.1 were excluded to reduce normalization-induced artifacts. Cell cycle assignment was performed by Seurat (v5.2.1),[70] using the marker genes from the HECA atlas.[30] Next, we used geometric sketching to subsample cells from each donor, using the interface to the geosketch algorithm[87] provided by the geosketch function from the sketchR R package (v1.2.0).[88] For each donor, we extracted 2,000 highly variable genes using the modelGeneVar function from scran, which were used to perform principal component analysis using the runPCA function from scater, based on which the geosketch function was applied to select 10% of the cells (or 150 cells, whichever of the two numbers was largest). If the donor contributed less than 150 cells, all of them were kept. Based on the sketched cells (n=5,700), a new set of 3,000 highly variable genes were defined using modelGeneVar. These genes were used to define principal components using the multiBatchPCA function from batchelor, onto which all cells were projected before batch correction was performed using the reducedMNN function from batchelor. The resulting reduced dimension representation was used as the basis for t-SNE[89] and UMAP projection, performed using the fitsne function from the snifter R package (v1.16.0)[90] and the umap function from the uwot R package (v0.2.2),[71] respectively. In both cases, the sketched cells were used to define the mapping to the low-dimensional space, which was then applied to the full set of cells via the project (snifter) and umap_transform (uwot) functions, respectively.

Clustering was performed on the sketched cells, using the clusterRows function from bluster, using a shared nearest neighbor graph (k=10, type="rank") and Leiden clustering with resolution 0.4.[91] Cluster labels for the remaining cells were defined by assigning the cluster label of the nearest neighbor among the sketched cells. Clusters were manually annotated into 14 final classes. This resolution parameters intentionally resulted into an initial over-clustering (44 clusters). Our rationale for using higher resolutions was to generate a more granular starting point from which clusters could be manually merged. Merging decisions were guided by (i) temporal emergence across the menstrual cycle; (ii) transcriptomic profiles and biological processes; and (iii) expression of well-established marker genes in literature. Finally, marker genes were calculated by comparing each pair of clusters using the pairwiseTTests function from scran, blocking on the sample and only considering upregulated genes, followed by calling combineMarkers with pval.type="all" to find specific marker genes. Only genes expressed in at least 0.05% of the cells were considered for the testing. Functional analysis of the top 100 marker genes for each cluster was performed using the gost function from the gprofiler2 R package (v0.2.3), using all tested genes as the universe and considering all gene sets from the GO:BP collection.[92]

The processed *in vivo* epithelial atlas was used to deconvolve the timecourse bulk RNA-seq data, using the BayesPrism package (v2.2.2).[72] Only protein-coding genes detected in at least 3 cells were considered, and marker genes were extracted using the BayesPrism functions get.exp.stat and select.marker with default settings.

scRNA-seq processing (*in vitro* organoid time course)

Time course scRNA-seq data generated for this study were quantified using Salmon (v1.9.0) and alevin-fry (v0.8.0),[58] in USA (unspliced-spliced-ambiguous) mode. Alevin-fry was run with parameters '-d fw –knee-distance' (for the generate-permit-list subcommand) and '–resolution cr-like-em –use-mtx' (for the quant subcommand). Initial quality control was performed using the alevinQC R package (v1.18.1).[59] Following quantification, the scRNA-seq data was processed following the same steps as the in vivo data described above, with a few differences. First, the initial selection of cells from the epithelial lineage was skipped, and all cells were retained for the main analysis. Second, no batch correction was performed, effectively excluding the steps above corresponding to the multiBatchNorm (replaced by logNormCounts), multiBatchPCA (replaced by calculatePCA) and reducedMNN functions (all cells were annotated to the same batch). Leiden clustering was performed with resolution 0.125 and clusters were manually annotated into 16 final classes. This resolution parameters intentionally resulted into an initial over-clustering (27 clusters). Our rationale for using higher resolutions was to generate a more granular starting point from which clusters could be manually merged. Merging decisions were guided by (i) temporal emergence across the menstrual cycle; (ii) transcriptomic profiles and biological processes; and (iii) expression of well-established marker genes in literature. In addition to the Seurat cell cycle annotation, tricycle was applied to obtain a continuous cell cycle position.[93] Sketching was applied to the full data set, extracting 10% of the cells (n=8,562).

Next, the SingleR R package (v2.8.0) was used to annotate the organoid time course data using the cell type labels defined in the in vivo atlas.[73] The aggregateAcrossCells function was used to build a set of reference profiles from the in vivo data, followed by application of the SingleR function to annotate the cells from the organoid time course.

Cell-cell communication analysis

To investigate potential interactions between cell populations from different lineages, we generated an *in vivo* atlas following the same steps as for the epithelial atlas described above, but without the subsetting to epithelial cells (we will refer to this as the 'all-lineage' endometrial atlas). In addition, no clustering was performed to assign cells to cell types. Instead, we proceeded in a stepwise manner. First, all cells that were part of the epithelial atlas were assigned the cell type label from there. Next, all remaining cells that were also part of the HECA were assigned the label from there (immune cells were assigned the fine-grained labels from the dedicated analysis of the immune lineage).[30] Finally, we used SingleR to predict labels for all remining cells, using the labelled cells as the reference data set.

Next, we subset the complete atlas to only samples from the menstrual and proliferative stages, and ran CellChat (v1.6.1) on this subset, following the workflow outlined in the package vignette.[74] Cell types with less than 100 cells were excluded, and only 'Secreted Signaling' interactions were included.

Generation of WNT7A knock-out organoid lines

EOs were collected and processed into single cell suspension as described in previous section. Nucleofection was performed with the D-Nucleofector (Lonza Bioscience, AAF-1003X) using the AMAXA P3 Primary Cell 4D-NucleofectorTM X Kit S (Lonza Bioscience, V4XP-3032). After centrifugation (6 minutes at 600 rcf), single cells were split in equal numbers per condition (~500,000 cells) and diluted in 20 μl P3 buffer (3.6 μl supplement and 16.4 μl solution per condition). Alt-R® S.p. HiFi Cas9 Nuclease V3 (IDT Lubioscience, 1081060) was diluted in PBS to a final concentration of 24.4 μM. Multi-sgRNAs were diluted in duplex buffer to a final concentration of 44.4 μM. SgRNA sequences can be found in Key Resources Table. Equal volumes of Cas9 nuclease and sgRNAs were mixed for 20 min at room temperature for the formation of ribonucleoprotein (RNP) complex. Per condition, 20 μl of cells resuspended in P3 buffer were mixed with 2 μl of the RNP complex. For enhanced KO efficiency, 1 μl of a non-specific template (100 μM stock concentration) was used. Cells were then loaded on the cassette for nucleofection. Nucleofected cells were washed with EOM, centrifuged (6 min, 600 rcf) and resuspended in cold Matrigel (Corning, 356231). For generation of KO clones, single EOs were picked, broken both with automatic pipette and manually and finally plated in 5 μl Matrigel droplets in a 96-well plate. Individual clones were expanded for downstream analysis.

RNA extraction

EOs were collected and Matrigel was removed using Cell Recovery Solution (Corning, 354253) for 50 min maximum on ice followed by one wash with cold PBS pH (7.4) (Gibco, 10010-015). Total RNA was extracted from organoid pellets using the RNeasy Micro kit with on column DNase treatment (Qiagen, 76004), following manufacturer's instructions. The RNA was resuspended in 14 μl RNase-free water. The purity and concentration of the RNA was determined using the UV-Vis Spectrophotometer NP80 (Implen).

cDNA synthesis

For cDNA synthesis, 500 ng to 1 μg of total RNA (depending on material availability) was reverse transcribed using SuperScript VILO cDNA Synthesis Kit (Thermo Fisher Scientific, 11754050) following manufacturer's instructions. The extracted RNA was diluted into 5X VILO Reaction Mix and 10X SuperScript III Enzyme Blend. The samples were then incubated for 10 minutes at 25°C, 1 hour at 42°C and 5 minutes at 85°C. An RNA sample without Reverse Transcriptase was used as control for genomic DNA contamination.

Real-time quantitative PCR (RT-qPCR)

RT-qPCR was performed with the StepOnePlus PCR system (Applied Biosystems) using TaqMan Fast Advanced Master Mix (Thermo Fisher Scientific, 4444557) and Taqman gene specific primer probes (*SCGB2A2*; Hs00935948, *FOXJ1*; Hs00230964, *MKI67*; Hs00606991, *WNT7A*; Hs00171699 from Thermo Fisher Scientific), following manufacturer's protocol. The cycling conditions followed were 20 seconds at 95°C and 40 cycles of 3 seconds at 95°C followed by 30 seconds at 60°C. Expression levels were calculated using the comparative Cycle threshold (Ct) method. The geometric means of *HPRT1* (Hs02800695), *TOP1* (Hs00243257), and *TBP* (Hs00427620) housekeeping genes were used for normalization of the relative gene expression levels. Normalized expression levels were calculated as $2^{-\Delta Ct}$ where $\Delta Ct = Ct_{\text{gene of interest}} - Ct_{\text{geometric mean of housekeeping genes}}$. Each RT-qPCR reaction was performed in technical duplicates, and a non-template control was always included.

Western Blotting

EOs were collected and Matrigel was removed using Cell Recovery Solution (Corning, 354253) for 50 min maximum on ice. EOs were then washed with cold PBS PH (7.4) (Gibco, 10010-015) and pellets were stored at -80°C. For lysis, pellets were resuspended in 500 μL RIPA lysis buffer (prepared in-house) supplemented with 1× Halt Protease Cocktail Inhibitor (Thermo Fisher Scientific, 1862209) and incubated on ice for 30 minutes. Lysates were centrifuged at 15,000×g for 20 minutes at 4°C, and the supernatant was collected for further analysis. Protein concentration was determined using the Pierce BCA Protein Assay Kit (Thermo Fisher Scientific, 23225) following manufacturer's instructions. Protein lysates (~10 μg) were diluted in 4× Laemmli SDS sample buffer (Thermo

Please cite this article in press as: Nikolakopoulou et al., An *in vitro* menstrual cycle using organoids captures epithelial cell transitions during menstruation and regeneration of the human endometrium, Cell Stem Cell (2026), https://doi.org/10.1016/j.stem.2026.04.005

Fisher Scientific, J63615) containing 50 mM DTT (Thermo Fisher Scientific, D9779). Samples were boiled for 5 minutes at 95°C and loaded into SDS-PAGE gels alongside a molecular weight standard. Proteins were transferred to nitrocellulose membranes (Bio-Rad, 1704158) using the Turbo Transfer System (25 V, 1.3 A, 7 minutes). Membranes were blocked with 1× TBST containing 5% milk (Biotium, 22012) for 1 hour at room temperature. Membranes were incubated overnight at 4°C with primary antibody WNT7A (Abcam, ab274321) (1:1000) diluted in 1× TBST containing 5% milk. Tubulin mouse antibody (Thermo Fisher Scientific, t5168 (1:2000) was used as loading control. Goat Anti-Rabbit, (Bio-Rad, 1706515) and anti-mouse (Bio-Rad, 1721011) secondary antibodies conjugated to HRP were diluted 1:5000 in 1× TBST with 5% milk and incubated for 45 minutes at room temperature. Membranes were washed twice with 1× TBST and developed using Amersham ECL Select™ detection reagent (Cytiva, RPN2235). Chemiluminescence was detected using the Amersham imaging system.

Luminex assay

Secreted protein concentrations were measured in conditioned media (supernatants) taken from EOs, derived from four independent donors, and subjected to the IVMC protocol. Supernatants from multiple wells corresponding to the same timepoint were pooled, aliquoted and stored in -80°C. Thawed aliquots were diluted 2X and assayed using a 46-plex Human Luminex Performance Assay (R&D Systems, LKTM014B) on a Bio-Rad Bio-Plex analyser, following manufacturer's instructions. Each sample was assayed in duplicate. Protein concentrations were interpolated from a standard curve of known concentrations of recombinant human proteins provided by the vendor, which was calculated with a five-parameter logistic non-linear regression model. The interpolated concentrations were normalized using the DNA concentration per well for each sample to account for the difference in confluency of EOs between timepoints and therefore the expected difference in the concentration of the analytes. Raw of all analytes measured can be found in Mendeley (DOI: 10.17632/vpmzzd54r5.1).

Wound healing assay

Endothelial cells were seeded into 2-well culture inserts (Ibidi, 80209) self-inserted into 24-well plates (TPP, 92024) at a density sufficient to achieve a confluent monolayer within 24h (30,000 HUtMECs and 20,000 HUVECs per well for each insert). Cells were pretreated for 3h before the onset of the assay, with EOM, or supernatants from EOs collected at Post-breakdown 24h. The inserts were then removed using tweezers allowing for the creation of a uniform 500 μm cell-free gap between the two cell layers. Detached cells were removed by gently washing the wells twice with Dulbecco's Phosphate Buffered Saline (DPBS). Fresh endothelial growth medium appropriate HUtMECs or HUVECs cell endothelial cell growth medium, EOM or supernatants from EOs were added accordingly. Each condition was assayed in triplicates. Brightfield imaging was performed with the 4x objective of the Incucyte Live-Cell Imaging and Analysis Instrument (Sartorius). Images of the same wound regions were acquired immediately after insert removal (0h) and every 30 min for a total of 24h.

Wound healing assay analysis

For image analysis, the Wound_healing_size_tool plugin ImageJ (version 1.51n) was used to quantify the wound area and wound coverage of the total area.[94] The percentage of cell-covered area relative to the total imaged area was calculated for each time point. Graphs visualizing cell-covered area as a function of time were generated using GraphPad Prism (version 10.2.0). The linear phase (the rate of gap closure remains constant) was then defined and a trend line for the linear phase was computed with a simple linear regression model. The slope of the trend line which corresponds to the rate of gap closure was then determined. The cell front velocity (V_{norm}) was then calculated using the following formula:

$$Vnorm = \frac{Rate\ of\ gap\ clocure}{Length\ of\ cell\ front\ x\ N}$$

where rate of gap closure is the rate at which the cell-covered area increases over time, length of cell front is the width of the image analysed, and N is the number of migrating cell fronts involved in closing the gap. For this assay, there are two converging cell fronts and therefore N equals 2. V_{norm} for each condition assayed in triplicates. To avoid interference from dead cells accumulating in the centre of the wound, each acquired image was split into two halves prior to analysis.

QUANTIFICATION AND STATISTICAL ANALYSIS

Data was plotted using GraphPad prism (version 10.2.0) and presented as the mean ± SD. For the comparison of *WNT7A* transcripts (Figure 3F), the number of spots, normalized to number of nuclei, from 14 image scans per condition was plotted. Significance value was determined using an unpaired t-test to compare the two groups (Hormonal Withdrawal 48h and Post-breakdown 24h). Statistical analyses of the Luminex (Figures 5D and S1G) and wound healing assay data (Figure 5F) were performed using the ordinary one-way ANOVA model (not paired, assuming Gaussian distribution of residuals and equal SDs) followed by Tukey's multiple comparison test. "n" represents the number of independent EO lines used to produce conditioned media and is indicated in the figure legends. Asterisks indicate significance level * $p \leq 0.05$, ** $p \leq 0.01$, *** $p \leq 0.001$, **** $p \leq 0.0001$. Differences with p values < 0.05 were regarded as significant.

Cell Stem Cell, Volume *33*

Supplemental Information

An *in vitro* menstrual cycle using organoids captures epithelial cell transitions during menstruation and regeneration of the human endometrium

Konstantina Nikolakopoulou, Weand Ybañez, Lhéanna Klaeylé, Lisa Frugoli, Tereza Cindrova-Davies, Hans-Rudolf Hotz, Charlotte Soneson, and Margherita Yayoi Turco

Supplemental information

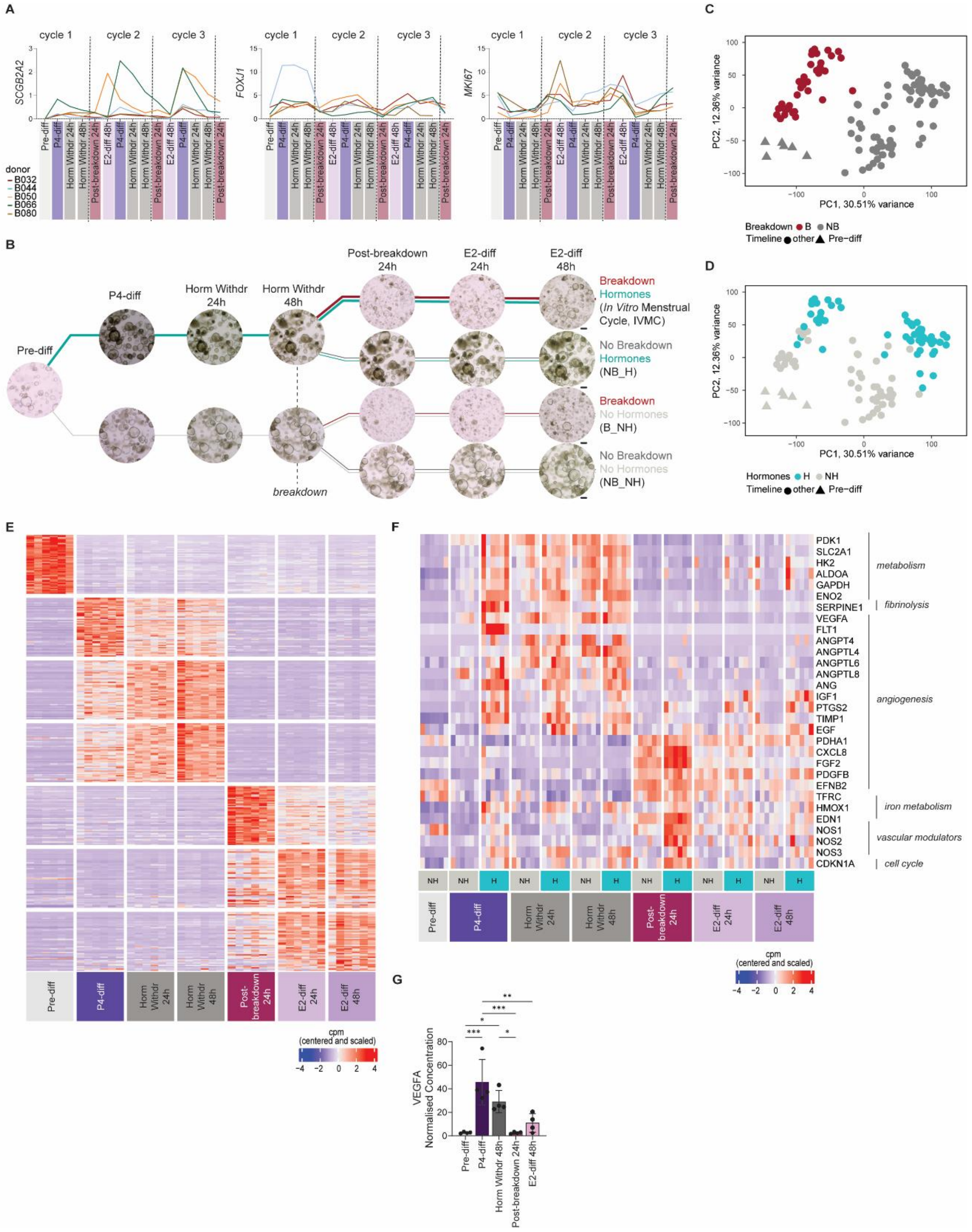

Figure S1. Bulk RNAseq of EOs undergoing the IVMC protocol, related to figure 1.

(**A**) qRT-PCR analysis of *SCGB2A2* (secretory marker), *FOXJ1* (ciliated marker), and *MKI67* (proliferative marker) expression from EOs undergoing continuous cycles of the IVMC protocol, normalised to housekeeping genes (n=5 independent EO lines). (**B**) Timeline of collection of EOs for bulk RNAseq (n=6 independent EO lines). The thicker lines represent the IVMC protocol. Control conditions include: EOs not broken down and treated with hormones (No Breakdown Hormones; NB_H); EOs broken down but not treated with hormones (Breakdown No Hormones; B_NH); or EOs neither broken down nor treated with hormones (No Breakdown No Hormones; NB_NH). Representative brightfield images for each timepoint are shown. Scale bar, 200 µm. (**C**) PCA of batch corrected samples from all conditions coloured by the breakdown variable. (**D**) PCA of batch corrected samples from all conditions coloured by the hormonal treatment variable. (**E**) Heatmap displaying the top 50 differentially upregulated genes from comparisons of each timepoint against all other timepoints using batch corrected samples from the IVMC protocol. (**F**) Heatmap depicting centered and scaled counts per million (cpm) of selected genes involved in hypoxia and angiogenesis-related processes across batch corrected samples in the IVMC protocol and control EOs broken down but not treated with hormones (B_NH). (**G**) Bar plot showing the normalised concentration of VEGFA analysed through a Luminex assay of supernatants of EOs subjected to the IVMC protocol (n=4 independent EO lines). Statistical analysis was performed using ordinary one-way ANOVA. Abbreviations: PC1 or PC2; Principal component 1 or 2, Pre-diff; Pre-differentiation, P4-diff; Progesterone differentiation, Horm Withdr; Hormonal Withdrawal, E2-diff; Estrogen differentiation

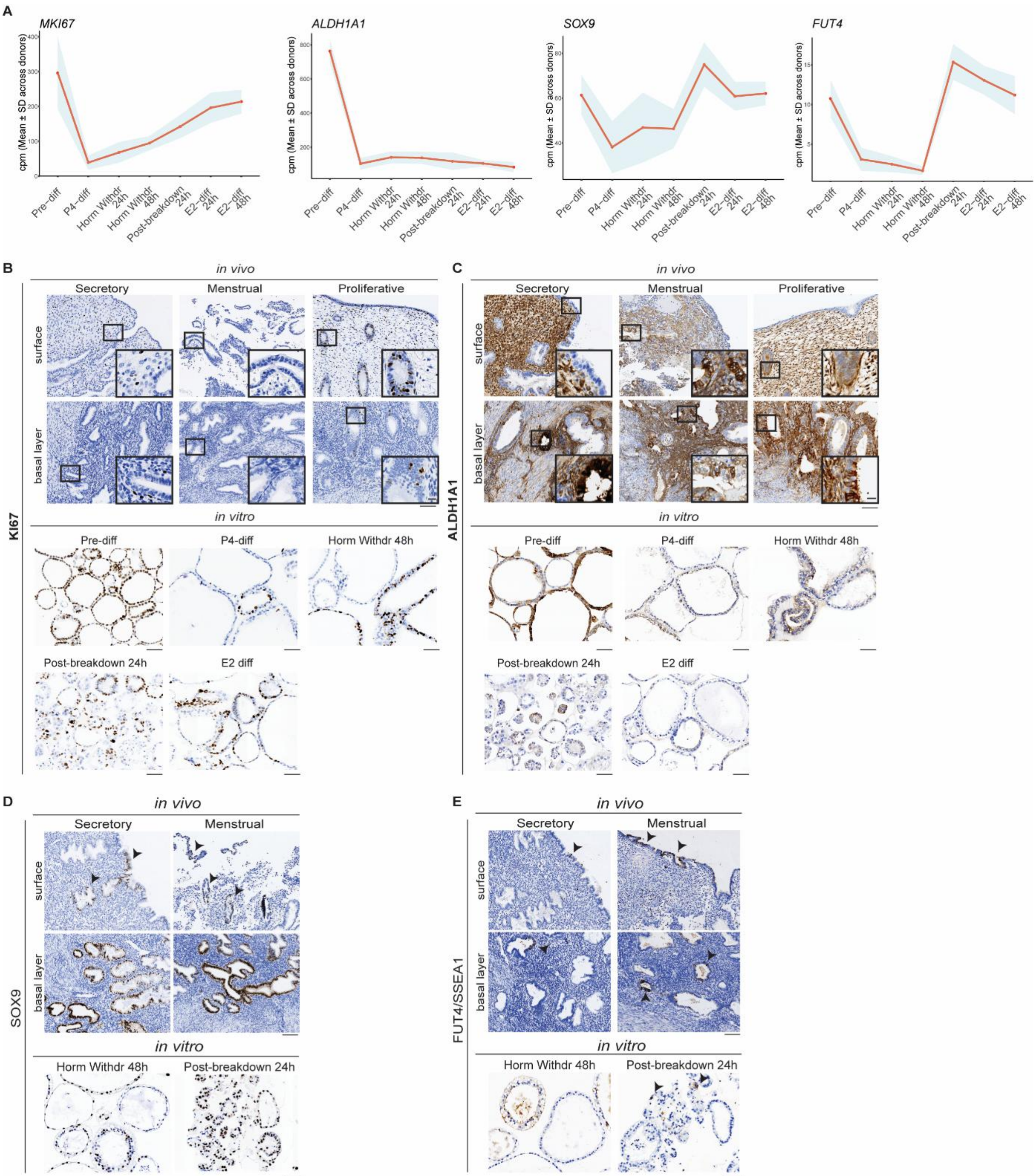

Figure S2: Characterisation of EOs at the Pre-diff phase of the IVMC protocol, related to figure 1.

(**A**) Line plots showing the mean expression levels in cpm of *MKI67*, *ALDH1A1*, *SOX9* and *FUT4* across the IVMC protocol. The red line represents the mean cpm values across donors (n=6 independent EO lines), while the shaded blue region indicates the standard deviation around the mean. (**B, C**) Representative IHC images for KI67 (B) and ALDH1A1 (C) in sections from secretory, menstrual, and proliferative endometrium (n=3 donors for each phase) and EOs across the IVMC protocol (n=4 independent EO lines). Black boxes indicate area shown at higher magnification (inset). Scale bars of tissue sections, 100 µm (main), 15 µm (inset). Scale bars of EO sections, 50 µm. (**D, E**) Representative IHC image for SOX9 (D), FUT4/SSEA1 (E) staining in sections from functional and basal layers of secretory and menstrual endometrium (n=3 donors for each phase) and EOs at Horm Withdr 48h and Post-breakdown 24h (n=4 independent EO lines). Black arrowheads indicate positive cells. Scale bars of tissue sections, 100 µm. Scale bars of EO sections, 50 µm.

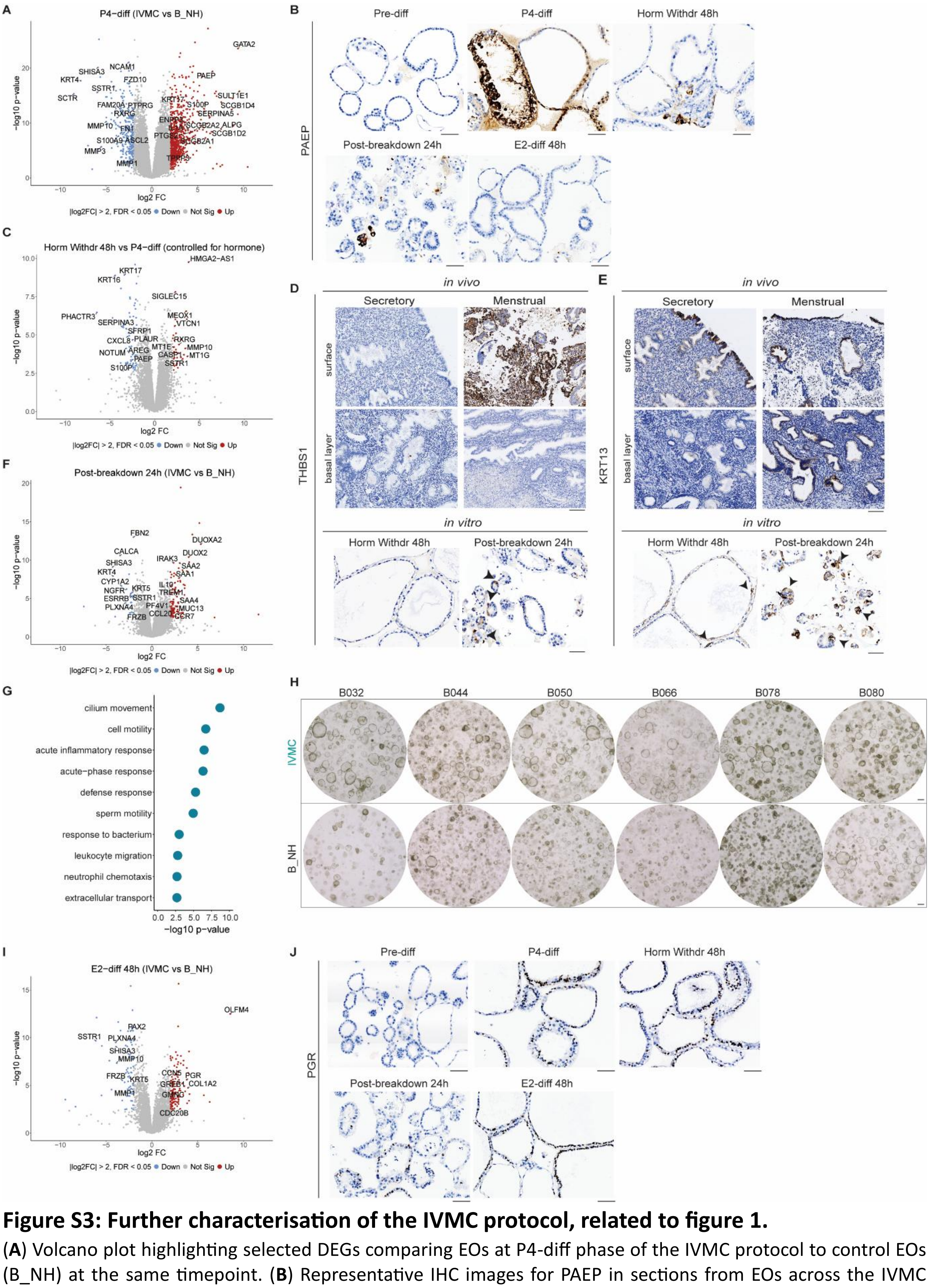

Figure S3: Further characterisation of the IVMC protocol, related to figure 1.

(**A**) Volcano plot highlighting selected DEGs comparing EOs at P4-diff phase of the IVMC protocol to control EOs (B_NH) at the same timepoint. (**B**) Representative IHC images for PAEP in sections from EOs across the IVMC protocol (n=4 independent EO lines). Scale bar, 50 µm. (**C**) Volcano plot highlighting selected DEGs comparing EOs of the IVMC protocol at P4-diff phase to EOs at Horm Withdr 48h corrected for control (NB_NH) conditions. (**D-E**) Representative IHC image for THBS1 (D), and KRT13 (E) staining in sections from functional and basal layers of secretory and menstrual endometrium (n=3 donors for each phase) and EOs at Horm Withdr 48h and Post-breakdown 24h (n=4 independent EO lines). Black arrowheads indicate positive cells. Scale bars of tissue sections, 100 µm. Scale bars of EO sections, 50 µm. (**F**) Volcano plot highlighting selected DEGs comparing EOs at Post-

breakdown 24h phase of the IVMC protocol to control EOs (B_NH) at the same timepoint. (**G**) Biological processes enriched in Post-breakdown 24h phase of the IVMC protocol using genes upregulated in F. (**H**) Brightfield images from 6 independent EO lines at E2-diff 48h phase of the IVMC protocol and control EOs (B_NH) at the same timepoint. Scale bar, 200 µm. (**I**) Volcano plot highlighting selected DEGs comparing EOs between E2-diff 48h phase of the IVMC protocol to control EOs (B_NH) at the same timepoint. (**J**) Representative IHC images for PGR in sections from EOs across the IVMC protocol (n=4 independent EO lines). Scale bar, 50 µm.
Abbreviations: B_NH; Breakdown No Hormones, NB_NH; No Breakdown No Hormones.

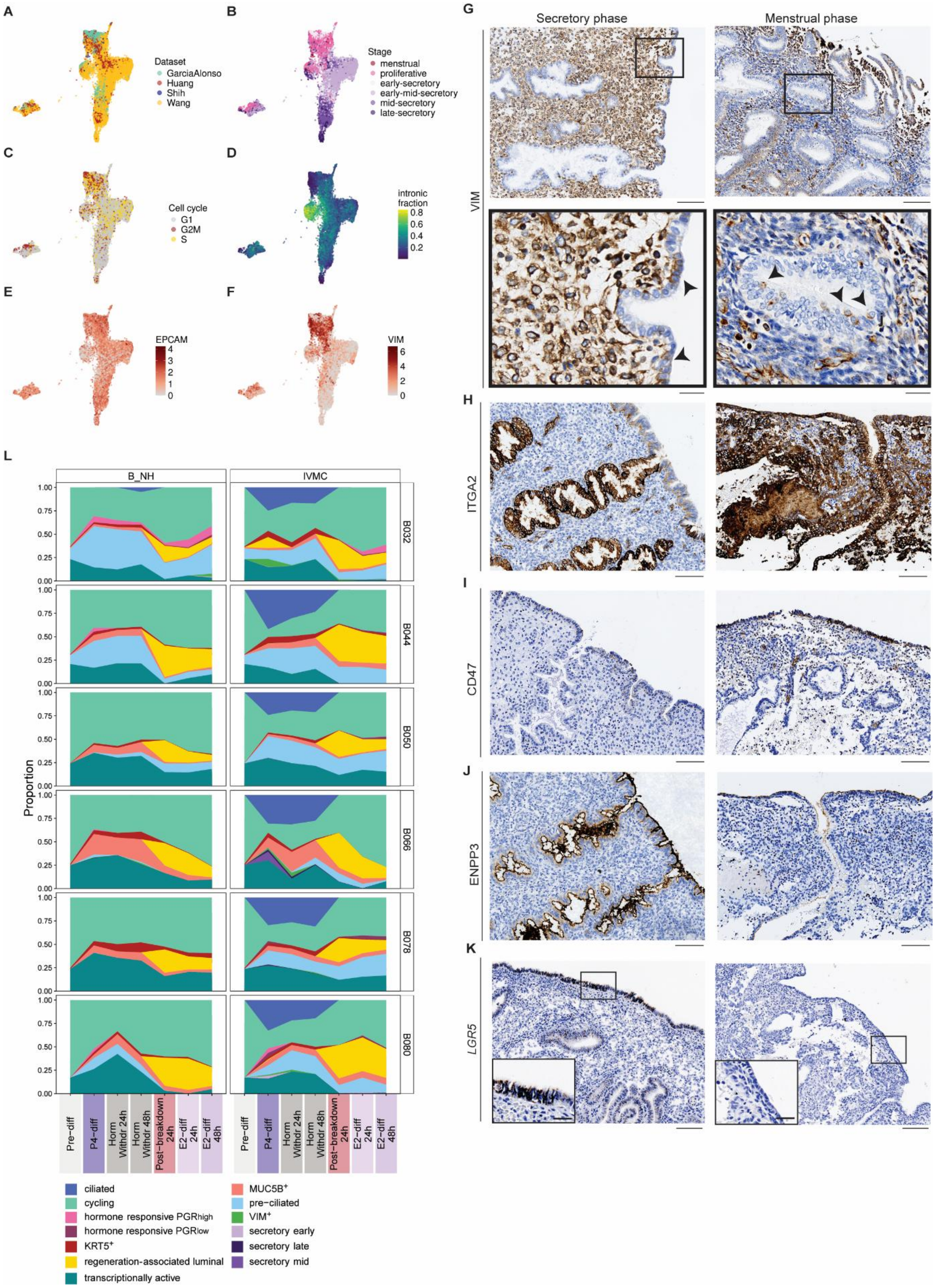

Figure S4 Description of epithelial cell populations *in vivo*, related to figure 2.

(**A-D**) UMAP visualization of epithelial cells from scRNAseq data of endometrial tissue coloured by the integrated datasets (A), stage of the menstrual cycle (B), cell cycle phase (C), and intronic fraction (D). (**E-F**) UMAP visualization showing the $\log_2$-transformed expression of *EPCAM* (E) and *VIM* (F) aross individual cells *in vivo*. (**G**) Representative IHC image for VIM in sections secretory and menstrual phase endometrium (n=3 donors for each phase). Scale bars, 100 µm (main), 20 µm (inset). (**H-J**) Representative IHC images for ITGA2 (H), CD47 (I) and ENPP3 (J) in sections from secretory and menstrual phase endometrium (n=3 donors for each phase). Scale bars, 100 µm. (**K**) *In situ* hybridization showing localization of *LGR5* transcripts in secretory and menstrual phase endometrium (n=1 donor for each phase). Scale bars, 100 µm (main), 50 µm (inset). (**L**) Area plots showing the relative abundance of the deconvolved *in vivo* epithelial cell clusters represented in EOs from each donor across the IVMC protocol and control condition B_NH; Breakdown No Hormones.

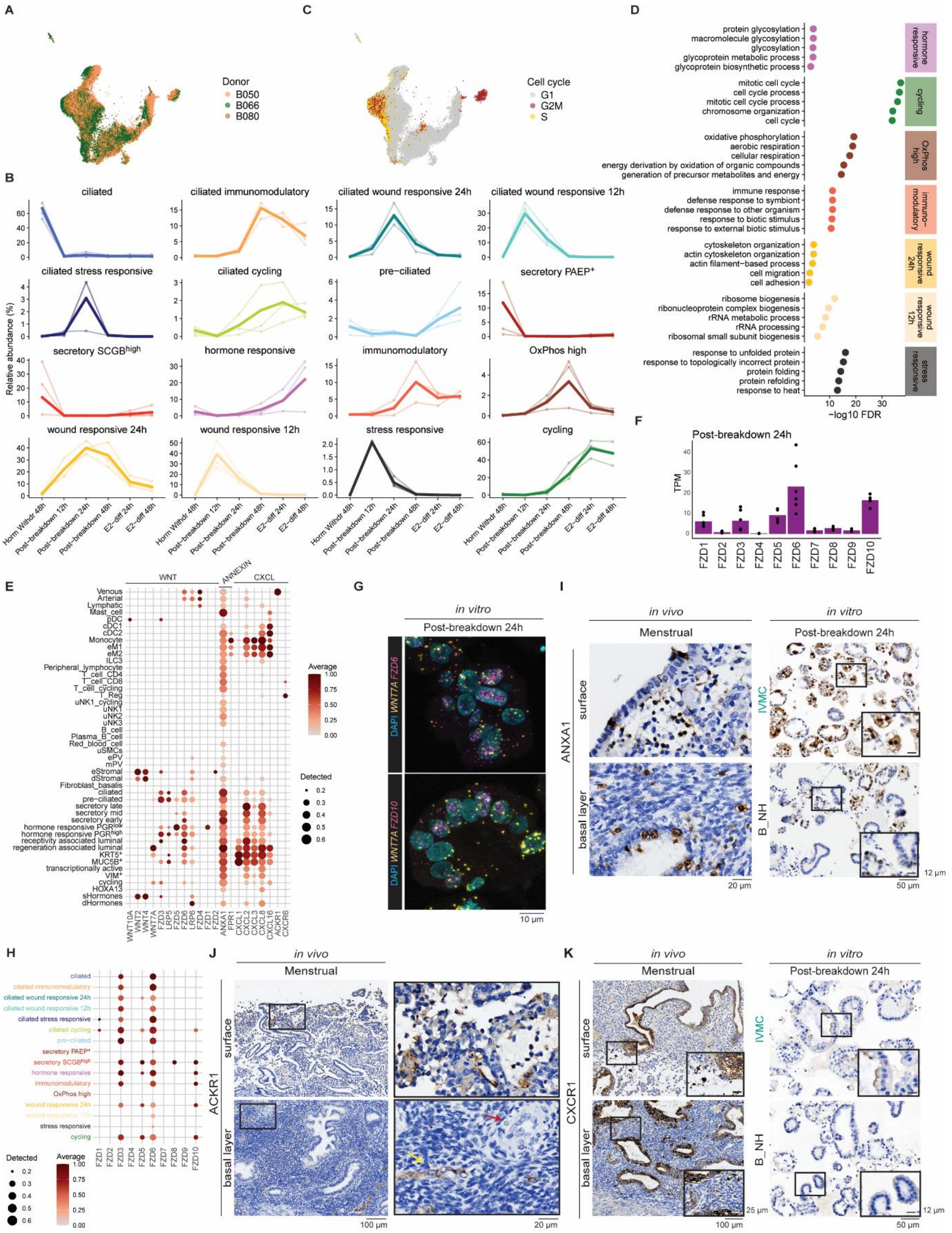

Figure S5: ScRNAseq analysis of EOs subjected to the IVMC protocol and further validation of ligands involved in crosstalk between epithelial and other cell types, related to figures 4 and 5.

(**A**) UMAP visualizations of epithelial cells in the IVMC protocol coloured for independent EO lines (**B**) Relative abundance plots of cell clusters across the different timepoints of the IVMC protocol. (**C**) UMAP visualizations of epithelial cells in the IVMC protocol coloured for the cell cycle stage. (**D**) Biological processes enriched in non-ciliated populations: stress responsive, wound responsive 12h, wound responsive 24h, immunomodulatory, OxPhos high, cycling and hormone responsive cell clusters. (**E**) Dot plot illustrating the expression of ligands and receptors involved in CXCL, Annexin, WNT and signalling networks. Dot size represents the proportion of expressing cells, while colour denotes log2-transformed expression levels, normalised across all cell populations. (**F**) Bar plot showing the average transcripts per million (TPM) of FZD receptors at Post-breakdown 24h in EOs undergoing the IVMC protocol analysed with bulk RNAseq. (**G**) Multiplex ISH for WNT7A (yellow) together with FZD6 or FZD10 (in magenta) in sections of EOs at Post-breakdown 24h. (**H**) Dot plot illustrating the expression of FZD receptors characteristic in each epithelial cell cluster in EOs subjected to the IVMC protocol analysed with scRNAseq. Dot size represents the proportion of expressing cells, while colour denotes log2-transformed expression levels, normalised across all cell populations. (**I**) Representative brightfield images for ANXA1 in sections from functional and basal layers of menstrual endometrium (n=3 donors) and EOs at Post-breakdown 24h (n=4 independent EO lines (**J**) Representative brightfield images for ACKR1 in sections from functional and basal layers of menstrual endometrium (n=3 donors). Yellow arrows point to veins and red arrows point to arteries. (**K**) Representative brightfield images for CXCR1 in sections from functional and basal layers of menstrual endometrium (n=3 donors) and EOs at Post-breakdown 24h (n=4 independent EO lines). Abbreviations: B_NH; Breakdown No Hormones.